Science Advances

AAAS

advances.sciencemag.org/cgi/content/full/2/3/e1501438/DC1

Supplementary Materials for

Direct and cost-efficient hyperpolarization of long-lived nuclear spin states on universal $^{15}N_2$-diazirine molecular tags

Thomas Theis, Gerardo X. Ortiz Jr., Angus W. J. Logan, Kevin E. Claytor, Yesu Feng, William P. Huhn, Volker Blum, Steven J. Malcolmson, Eduard Y. Chekmenev, Qiu Wang, Warren S. Warren

Published 25 March 2016, *Sci. Adv.* **2**, e1501438 (2016)
DOI: 10.1126/sciadv.1501438

The PDF file includes:

- Synthesis of $^{15}N_2$-diazirine and iridium precatalyst
- Theoretical derivation of resonance conditions for hyperpolarization transfer
- Spin dynamics during low- to high-field sample transfer
- MD simulations of possible transitions states for hyperpolarization transfer
- Sample preparation and setup to obtain well-controlled milligauss fields
- Hyperpolarization buildup dynamics, lifetimes, and enhancements in detail
- Appendix
- Fig. S1. Synthesis of 2-cyano-3-(3′-(methyl-d_3)-3′*H*-diazirine-3′-yl-1′,2′-$^{15}N_2$)propanoic acid using modified literature procedures.
- Fig. S2. Spin system for polarization transfer.
- Fig. S3. Eigenstates of a *J*-coupled two-spin system as a function of magnetic field.
- Fig. S4. Simulated spectra for magnetization and singlet order.
- Fig. S5. Three candidate conformations of 2-cyano-3-(D_3-methyl-$^{15}N_2$-diazirine)-propanoic acid as identified by DFT PBE + TS calculations, as used to construct likely catalytically active structures producing hyperpolarization attached to the SABRE catalyst.
- Fig. S6. First-principles derived candidate conformations of catalytic species that drive hyperpolarization transfer.
- Fig. S7. Experimental SABRE-SHEATH setup.
- Fig. S8. Decay time constants, buildup constants, and enhancements as function of magnetic field and concentrations.

- Fig. S9. The effect of continued singlet-polarization buildup after stopping p-H_2 bubbling.
- Table S1. Relative energies of the diazirine attachment modes tested in this work for the case of two different ligands that are simultaneously present: two equatorial hydrides, axial IMes, axial pyridine, one equatorial pyridine, and diazirine in an equatorial position.
- Table S2. Relative energies of the diazirine attachment modes tested in this work for the case of two diazirine molecules that are simultaneously present.
- Table S3. Magnetization lifetimes, T_1, under varying catalyst concentrations and holding fields.
- Table S4. Singlet lifetimes, T_S, under varying catalyst concentrations and holding fields.
- Table S5. Magnetization buildup times, Tb_1, at 6 mG under varying catalyst concentrations.
- Table S6. Singlet buildup times, Tb_S, under varying catalyst concentrations and magnetic fields.
- Table S7. Enhancements, ε, under varying concentrations of catalyst [IrCl(COD)(IMes)] (**1a**), [Ir(COD)(IMes)(Py)][PF_6] (**1b**), diazirine substrate (**2**), pyridine (**3**), and D_2O (**4**).
- References (*55–69*)

1) Synthesis of $^{15}N_2$-diazirine and iridium precatalyst

Supplementary Materials and Methods

General Experiment Information.

Unless otherwise noted, reactions were performed without exclusion of air or moisture. All commercially available reagents and solvents were used as received unless otherwise stated. THF was obtained from a DriSolve purification system when necessary. *n*-BuLi was titrated using 1,3-diphenyl-2-propanone tosylhydrazone directly before use. CD_3I was distilled under N_2 before use. ^{15}N-labled hydroxylamine *O*-sulfonic acid ($^{15}NH_2OSO_3H$) was synthesized from ^{15}N-labeled hydroxylamine hydrochloride and chlorosulfonic acid directly before use (*69*). Analytical thin-layer chromatography (TLC) was performed using aluminum plates pre-coated with 0.25 mm of 230–400 mesh silica gel impregnated with a fluorescent indicator (254 nm). TLC plates were visualized by exposure to ultraviolet light and/or various stains. Organic solutions were concentrated *in vacuo* using a rotary evaporator. Column chromatography was performed with silica gel (60 Å, standard grade).

NMR spectra were recorded on Varian iNova 400 and 500 spectrometers. Proton and carbon chemical shifts (δ_H, δ_C) are quoted in *ppm* and referenced to $SiMe_4$ with residual protonated solvent as internal standard. For chloroform-*d*, solvent residuals are 7.26 ppm and 77.16 ppm for proton and carbon respectively. Resonances are described as s (singlet), d (doublet), t (triplet), q (quartet) and combinations thereof. Coupling constants (*J*) are given in *Hz* and rounded to the nearest 0.1. For diastereotopic protons, no particular stereochemistry is implied.

High resolution mass spectra were recorded by the Mass Spectrometry Facility at the Department of Chemistry, Duke University on an Agilent 6224 TOF LC/MC. High resolution *m*/*z* values are reported in Daltons, calculated to 4 d.p. from the molecular formula. All found values are within 5 ppm tolerance.

Infrared spectra were recorded on a ThermoScientific Nicolet 6700 FTIR equipped with a diamond ATR. Absorption maxima (ν_{max}) are described as s (strong), m (medium), w (weak), and br (broad) and are quoted in wavenumbers (cm^{-1}). Only selected peaks are reported.

The synthesis of 2-Cyano-3-(3’-(methyl-d3)-3’H-diazirin-3’-yl-1’,2’-$^{15}N_2$)propanoic acid is detailed in Fig. S1 and achieved by modified literature procedures (*56*-*60*).

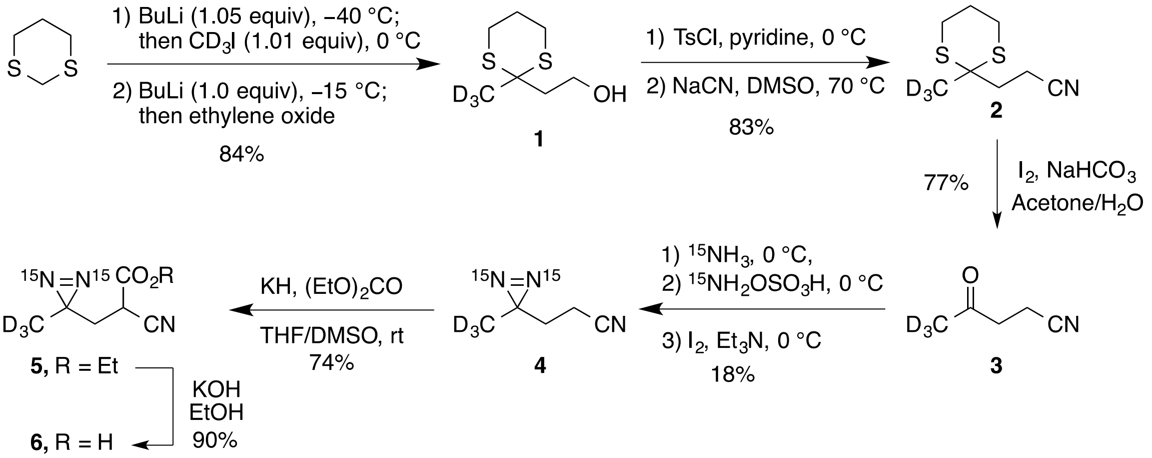

fig. S1. Synthesis of 2-cyano-3-(3'-(methyl-*d*$_3$)-3'*H*-diazirin-3'-yl-1',2'-$^{15}N_2$)propanoic acid using modified literature procedures.

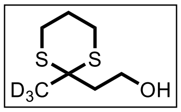

2-(2'-(Methyl-*d*$_3$)-1',3'-dithian-2'-yl)ethan-1-ol (1). To a solution of 1,3-dithiane (3.97 g, 33 mmol, 1.0 equiv) in THF (60 mL) under a N_2 atmosphere at -40 °C, was added dropwise *n*-BuLi (13.9 mL, 2.5 M in hexanes, 34.65 mmol, 1.05 equiv) over 10 min. The reaction was slowly warmed to 0 °C, followed by the dropwise addition of CD_3I over 10 min. The reaction was allowed to stir at 0 °C for 4 h and then at 25 °C for 10 h, and then was cooled back down to -15 °C. To the reaction mixture, *n*-BuLi (13.2 mL, 33 mmol, 1.0 equiv, 2.5 M in hexanes) was added dropwise over 10 min followed by a solution of ethylene oxide (11 mL, 2.5–3.3 M in THF, 27.5–36.3 mmol, 0.83–1.1 equiv). The reaction was allowed to warm to 25 °C over 1.5 h, then quenched with aqueous HCl (20 mL, 2 M), and extracted with Et_2O (2 × 100 mL). The organic layers were combined, washed with a saturated solution of $NaHCO_3$ (100 mL), brine (2 × 50 mL), dried over Na_2SO_4, and filtered. The filtrate was concentrated *in vacuo*. The crude residue was purified by flash column chromatography (20% ethyl acetate–hexanes to 50% ethyl acetate–hexanes) to give **1** as a light yellow liquid (4.97 g, 84%). **R*f*** = 0.22 (25% ethyl acetate–hexanes); **^{1}H NMR** (400 MHz, $CDCl_3$, see appendix, Fig. S10): **δ** 3.84 (t, *J* = 5.9, 2H), 2.99 (ddd, *J* = 14.7, 10.1, 3.0, 2H), 2.80 (ddd, *J* = 14.7, 6.6, 3.2, 2H), 2.29 (s, br, 1H), 2.27 (t, *J* = 5.9, 2H), 2.04 (dtt, *J* = 14.0, 6.6, 3.0, 1H), 1.90 (dtt, *J* = 14.0, 10.1, 3.2, 1H); **^{13}C NMR** (100 MHz, $CDCl_3$, see appendix Fig. S11): **δ** 58.6, 46.7, 42.5, 26.0 (2C), 24.4, (note that a carbon peak for CD_3 could not be found); **FTIR** (thin film), cm^{-1} 3373 (br), 2904, 1421, 1275, 1042, 905; **HRMS-ESI** (m/z) calcd. for $C_7H_{12}D_3OS_2$ ($[M+H]^+$): 182.0747; found: 182.0743.

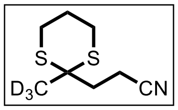

3-(2’-(Methyl-d_3)-1’,3’-dithian-2’-yl)propanenitrile (2). To a solution of **1** (4.90 g, 27 mmol, 1.0 equiv) in pyridine (25 mL) at 0 °C, was added TsCl (5.40 g, 28.35 mmol, 1.05 equiv) portion wise over 15 min. The reaction was stirred at 0 °C for 2 h then was placed in a -20 °C freezer for 24 h. The reaction was warmed and added to a mixture of aqueous concentrated HCl (50 mL) and ice (200 g). The reaction mixture was extracted with Et_2O (250 mL). The organic layer was washed with cold aqueous HCl (2 × 50 mL, 0.5 M), cold aqueous NaOH (50 mL, 0.5 M), a saturated aqueous solution of $NaHCO_3$ (25 mL), and brine (25 mL). The solvent was removed *in vacuo*. To the residue was added DMSO (60 mL) followed by NaCN (2.65 g, 54 mmol, 2.0 equiv), and the solution was heated to 70 °C for 4 h. After cooling down to 25 °C, the reaction mixture was added H_2O (75 mL) and then was extracted with Et_2O (3 × 60 mL). The organic layers were combined, washed with aqueous NaOH (2 × 40 mL, 1 M), brine (40 mL), dried over Na_2SO_4, and filtered. The filtrate was concentrated *in vacuo*. The crude residue was purified by flash column chromatography (10% ethyl acetate–hexanes to 25% ethyl acetate–hexanes) to give **2** as a clear liquid (4.26 g, 83%). R_f = 0.44 (25% ethyl acetate–hexanes); **^{1}H NMR** (400 MHz, $CDCl_3$, see appendix, Fig. S12): **δ** 2.89 (ddd, J = 14.8, 10.2, 3.0, 2H), 2.77 (ddd, J = 14.8, 6.4, 3.3, 2H), 2.54 (t, J = 8.0, 2H), 2.33 (t, J = 8.0, 2H), 2.03 (dtt, J = 14.0, 6.4, 3.0, 1H), 1.89 (dtt, J = 14.0, 10.2, 3.3, 1H); **^{13}C NMR** (126 MHz, $CDCl_3$, see appendix, Fig. S13): **δ** 119.5, 47.2, 36.3, 26.3 (2C), 24.4, 13.3, (note that a carbon peak for CD_3 could not be found); **FTIR** (neat), cm^{-1} 2907, 2244, 1421, 1277, 1039, 908; **HRMS-ESI** (m/z) calcd. for $C_8H_{11}D_3NS_2$ ($[M+H]^+$): 191.0750; found: 191.0751.

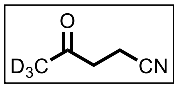

4-Oxopentanenitrile-5,5,5-d_3 (3). To a solution of **2** (4.00 g, 21 mmol, 1.0 equiv) in acetone/H_2O (75 mL / 7.5 mL) at 0 °C was added solid $NaHCO_3$ (12.35 g, 147 mmol, 7 equiv) followed by I_2 (15.99 g, 63 mmol, 3 equiv). The reaction was stirred at 0 °C for 2 h and then warmed to 25 °C. An additional amount of I_2 (5.33 g, 21 mmol, 1.0 equiv) was added and the reaction stirred for 1 h. Then to the reaction mixture, was added an aqueous solution of $Na_2S_2O_3$ (250 mL, 10% w/v). The resulting solution was extracted with EtOAc (4 × 200 mL). The organic layers were combined, washed with an aqueous solution of $Na_2S_2O_3$ (40 mL, 10% w/v), an aqueous solution of NaOH (80 mL, 1 M), brine (100 mL), dried over Na_2SO_4, and filtered. The filtrate was concentrated *in vacuo*. The crude residue was purified by flash column chromatography (10% ethyl acetate–hexanes to 50% ethyl acetate–hexanes) to give **3** as a light yellow liquid (1.62 g, 77%). **R_f** = 0.14 (25% ethyl acetate–hexanes); **^{1}H NMR** (400 MHz, $CDCl_3$, see appendix, Fig. S14): **δ** 2.83 (t, J = 7.2, 2H), 2.58 (t, J = 7.2, 2H); **^{13}C NMR** (126 MHz, $CDCl_3$, see appendix, Fig. S15): **δ** 204.0, 118.8, 37.5, 27.8 (septet, $^1J_{D\text{–}C}$ = 19.5), 10.5; **FTIR** (neat), cm^{-1} 2249, 1710, 1412, 1360, 1175; Satisfactory HRMS data could not be obtained. **GCMS** (m/z) calcd. for $C_5H_4D_3NO$ (M): 100.1; found: 100.1.

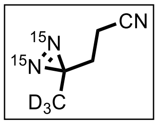

3-(3’-(Methyl-d_3)-3’*H*-diazirine-3’-yl-1’,2’-$^{15}N_2$)propanenitrile (4). To a solution of **3** (1.50 g, 15 mmol, 1.0 equiv) in aqueous $^{15}NH_4OH$ (2.7 mL, 37.5 mmol, 2.5 equiv, 14 M) at 0 °C, was added dropwise a solution of $^{15}NH_2OSO_3H$ (1.71 g, 15 mmol, 1.0 equiv) in MeOH (9 mL) over 5 min. The reaction was stirred at 0 °C for 40 min and then at room temperature for 1 h. The reaction was poured onto MeOH (60 mL), and filtered. The solvent was removed *in vacuo* (~20 mL residue). The concentrated solution was cooled at 0 °C and Et_3N (1 mL) was added, followed by the portion wise addition of I_2 (until a brown color persisted). The reaction was stirred for an additional 40 min at 0 °C, then at 25 °C for 30 min, and was quenched by the addition of brine (50 mL). The mixture was extracted with Et_2O (2 × 25 mL). The organic layers were combined, washed with aqueous solution of $Na_2S_2O_3$ (2 × 25 mL, 10% w/v), aqueous HCl (2 × 10 mL, 0.25 M), saturated aqueous $NaHCO_3$ (2 × 10 mL), and then brine (10 mL). The organic layer was dried over Na_2SO_4, and filtered. The filtrate was concentrated *in vacuo*. The crude residue was purified by flash column chromatography (10% ethyl acetate–hexanes to 50% ethyl acetate–hexanes) to give **4** as a clear liquid (0.303 g, 18%). $\mathbf{R_f}$ = 0.50 (25% ethyl acetate–hexanes); $\mathbf{^1H}$ **NMR** (400 MHz, $CDCl_3$, see appendix, Fig. S16): **δ** 2.23 (t, J = 7.5, 2H), 1.75 (t, J = 7.5, 2H); $\mathbf{^{13}C}$ **NMR** (126 MHz, $CDCl_3$, see appendix, Fig. S17): **δ** 118.4, 30.7, 24.2 (t, $^1J_{15N–C}$ = 9.0), 18.4 (septet, $^1J_{D–C}$ = 19.2), 12.1; **FTIR** (neat), cm^{-1} 2251, 1538, 1445, 1426, 755; Satisfactory HRMS data could not be obtained. Satisfactory GCMS data could not be obtained.

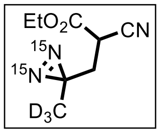

Ethyl 2-cyano-3-(3'-(methyl-*d*$_3$)-3'*H*-diazirine-3'-yl-1',2'-^{15}*N*$_2$)propanoate (5). To a stirring suspension of KH (90 mg, 2.25 mmol, 5 equiv, prepared by washing 30 wt % KH dispersed in mineral oil with pentanes) in anhydrous THF (0.5 mL), was added diethyl carbonate (0.22 mL, 1.8 mmol, 4 equiv) and DMSO (0.04 mL) under a N_2 atmosphere. A solution of **4** (52 mg, 0.45 mml, 1.0 equiv) in THF (0.5 mL) was then added dropwise to the reaction over 20 min and the resulting solution was stirred overnight. The reaction was quenched with the addition of a saturated aqueous solution of NH_4Cl (2 mL) followed by aqueous HCl (5 mL, 2 M). The reaction mixture was extracted with EtOAc (3 × 7.5 mL). The organic layers were combined, washed with brine (5 mL), dried over Na_2SO_4, and filtered. The filtrate was concentrated *in vacuo*. The crude residue was purified by flash column chromatography (10% ethyl acetate–hexanes) to give **5** as a clear liquid (62 mg, 74%). $\mathbf{R_f}$ = 0.54 (25% ethyl acetate–hexanes); $\mathbf{^1H}$ **NMR** (400 MHz, $CDCl_3$, see appendix, Fig. S18): **δ** 4.30 (q, J = 7.2, 2H), 3.37 (dd, J = 8.1, 6.5, 2H), 2.04 (ddt, J = 15.0, 8.1, $^3J_{15N–H}$ = 0.6, 1H), 1.99 (ddt, J = 15.0, 6.5, $^3J_{15N–H}$ = 0.6, 1H), 1.34 (t, J = 7.2, 3H); $\mathbf{^{13}C}$ **NMR** (126 MHz, $CDCl_3$, see appendix, Fig. S19): **δ** 164.8, 115.7, 63.2, 35.2, 32.5, 23.2 (t, $^1J_{15N–C}$ = 9.1), 19.4–18.2 (m, CD_3), 13.7; **FTIR** (thin film), cm^{-1} 1745, 1262, 1213, 1030; **HRMS-ESI** (m/z) calcd. for $C_8H_9D_3N^{15}N_2O_2$ ($[M+H]^+$): 187.1053; found: 187.1053.

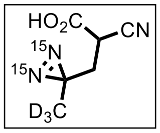

2-Cyano-3-(3'-(methyl-*d*$_3$)-3'*H*-diazirine-3'-yl-1',2'-^{15}*N*$_2$)propanoic acid (6). To a stirring solution of **5** (60.0 mg, 0.32 mmol, 1.0 equiv) in EtOH (1 mL, 190 proof) was added dropwise a solution of KOH (53.9 mg, 0.96 mmol, 3 equiv) in EtOH (1 mL, 190 proof) over 3 min. The reaction was stirred for 24 h and was then concentrated *in vacuo*. To the residue was added H_2O (5 mL). The solution was washed with Et_2O (5 mL). The aqueous layer was acidified with aqueous HCl (5 mL, 2 M) and extracted with Et_2O (3 × 7.5 mL). The organic layers were combined, dried over Na_2SO_4 and filtered. The filtrate was concentrated *in vacuo* to give **6** as a green oil (45.7 mg, 90%). $\mathbf{R_f}$ = 0.35 (5% methanol–dichloromethane); $\mathbf{^1H}$ **NMR** (500 MHz, $CDCl_3$, see appendix, Fig. S20): **δ** 8.22 (s, br, 1H), 3.47 (dd, J = 8.3, 6.1, 1H), 2.09 (ddt, J = 15.0, 8.3, $^3J_{15N–H}$ = 0.6, 1H), 2.03 (ddt, J = 15.0, 6.1, $^3J_{15N–H}$ = 0.6, 1H); $\mathbf{^{13}C}$ **NMR** (126 MHz, $CDCl_3$, see appendix Fig. S21): **δ** 169.7, 115.2, 35.1, 32.6, 23.2 (t, $^1J_{15N–C}$ = 8.8), 19.2–18.4 (m, CD_3); **FTIR** (thin film), cm^{-1} 3502 (br), 2924 (br), 2360, 1739, 1263 (br), 1216 (br); **HRMS-ESI** (m/z) calcd. for $C_6H_3D_3N^{15}N_2O_2$ ($[M-H]^-$): 157.0594; found: 157.0593.

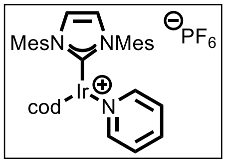

(1,5-Cyclooctadiene)(pyridine)(1,3-(2,4,6-trimethylphenyl) imidazol-2-ylidene)iridium(I) hexafluorophosphate. To a stirred solution of (1,5-cyclooctadiene)(2,3-(2,4,6-trimethylphenyl)imidizol-2-ylidene)iridium(I) chloride (96.0 mg, 150 μmol, 1.00 equiv) in MeOH (6.0 mL) was added pyridine (75 μL, 960 μmol, 6.40 equiv). The solution was stirred at 22 °C for 1 h, and then NH_4PF_6 (83.1 mg, 510 μmol, 3.40 equiv) was added as a single portion. The solution was stirred for a further 1 h, and the solvent was removed *in vacuo*. The residue was purified by flash column chromatography (0.5→2% MeOH in CH_2Cl_2), which gave the title compound (107 mg, 128 μmol, 85%) as an orange solid; **^{1}H NMR** (500 MHz, $CDCl_3$, see appendix, Fig. S22) δ 7.80–7.73 (m, 3H, py $H_{2,4,6}$), 7.25 (t, J = 5.6, 2H, py $H_{3,5}$), 7.14–6.91 (m, 6H, N*H*C=C*H*N & MesC*H*), 3.64–3.58 (m, 2H, C*H*=C*H* *trans* to IMes), 3.27–3.21 (m, 2H, C*H*=C*H* *trans* to pyridine), 2.44 (s, 6H, Mes *p*-CH_3), 2.27–1.78 (br, 16H, cod CH_2 & Mes *o*-CH_3), 1.70–1.52 (m, 4H, cod CH_2); **^{13}C NMR** (126 MHz, $CDCl_3$, see appendix Fig. S23) δ 173.6, 150.5, 140.2, 137.9, 135.5, 135.4, 129.8, 126.3, 125.1, 82.5, 65.1, 32.7, 29.4, 21.2, 18.3; **^{19}F NMR** (376 MHz, $CDCl_3$, see appendix) δ -73.6 (d, $^1J_{FP}$ = 712); **^{31}P NMR** (162 MHz, $CDCl_3$) δ -144.4 (sept, $^1J_{PF}$ = 712); **HRMS-ESI** (m/z) calc. for $C_{29}H_{36}IrN_2$ ([M-pyridine-Cl]$^+$): 605.2502; found 605.2499. *Data are consistent with literature values* (*61*).

2) Theoretical derivation of resonance conditions for hyperpolarization transfer

The polarization transfer occurs in an AA′BB′ spin system as illustrated in Fig. 3B of the main manuscript. Here, in Fig. S2, we simplify the sketch to highlight the important interactions, which are the J-couplings and the frequency difference, ν_H-ν_N, between parahydrogen derived protons and the diazirine nitrogen-15.

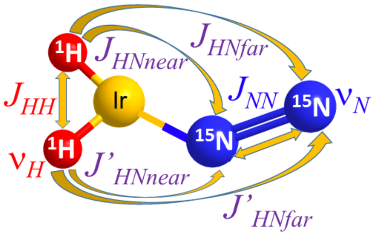

$$\Delta J_{near} = J_{HNnear} - J'_{HNnear}$$
$$\Delta J_{far} = J_{HNfar} - J'_{HNfar}$$
$$\Sigma J_{near} = J_{HNnear} + J'_{HNnear}$$
$$\Sigma J_{far} = J_{HNfar} + J'_{HNfar}$$

fig. S2. Spin system for polarization transfer. In the depicted AA’BB’ spin system polarization is transferred from the hydrides to the $^{15}N_2$-diazirine. The important interactions are depicted. All possible J-couplings may have different values, however it is assumed that hyperpolarization is performed at a low enough magnetic fields such that the frequency of both hydrides is equal to one frequency ν_H and that the frequency of both nitrogens is equal to one frequency ν_N.

The initial state is the parahydrogen singlet state on the H spins. This state will evolve under the Hamiltonian of the AA′BB′ system. The Hamiltonian contains the magnetic field-dependent frequencies ν_H and ν_N and the magnetic field-independent J-couplings. Lastly, we associate the spins A, A′, B and B′ with the spin operators $\mathbf{I}_H$, $\mathbf{I}'_H$, $\mathbf{I}_N$ and $\mathbf{I}'_N$.

With this notation the Hamiltonian is expressed as:

$$\begin{aligned} H = \nu_H \left(I_{Hz} + I'_{Hz} \right) + \nu_N \left(I_{Nz} + I'_{Nz} \right) \\ + J_{HH}\, \mathbf{I_H I'_H} + J_{NN}\, \mathbf{I_N I'_N} \\ + J_{NHnear}\, \mathbf{I_H I_N} + J_{NHnear} \mathbf{I'_H I_N} + J_{NHfar}\, \mathbf{I_H I'_N} + J_{NHfar} \mathbf{I'_H I'_N} \end{aligned} \quad . \qquad \text{(S1)}$$

It is now convenient to introduce the sum and the difference of the NH-*J*-couplings (also depicted in Fig. S2),

$$\begin{aligned} \Delta J_{near} &= J_{HNnear} - J'_{HNnear} \\ \Delta J_{far} &= J_{HNfar} - J'_{HNfar} \\ \Sigma J_{near} &= J_{HNnear} + J'_{HNnear} \\ \Sigma J_{far} &= J_{HNfar} + J'_{HNfar} \end{aligned} \quad , \qquad \text{(S2)}$$

and to rewrite Eq. S1 as:

$$\begin{aligned} H = \nu_H \left(I_{Hz} + I'_{Hz} \right) + \nu_N \left(I_{Nz} + I'_{Nz} \right) \\ + J_{HH}\, \mathbf{I_H I'_H} + J_{NN}\, \mathbf{I_N I'_N} \\ + \frac{\Sigma J_{near}}{2} (\mathbf{I_H I_N} + \mathbf{I'_H I_N}) \\ - \frac{\Delta J_{near}}{2} (\mathbf{I_H I_N} - \mathbf{I'_H I_N}) \\ + \frac{\Sigma J_{far}}{2} (\mathbf{I_H I'_N} + \mathbf{I'_H I'_N}) \\ - \frac{\Delta J_{far}}{2} (\mathbf{I_H I'_N} - \mathbf{I'_H I'_N}) \end{aligned} \qquad \text{(S3)}$$

The further analysis is best performed in a specific matrix representation of this Hamiltonian. A matrix representation requires a specific basis and the most adequate basis for the problem at hand is the Singlet-Triplet basis for coupled spin pairs, where

$$\begin{gathered} S_0 = \frac{1}{\sqrt{2}} \left| \uparrow\downarrow \right\rangle - \left| \downarrow\uparrow \right\rangle; \\ T_+ = \left| \uparrow\uparrow \right\rangle; \quad T_0 = \frac{1}{\sqrt{2}} \left| \uparrow\downarrow \right\rangle + \left| \downarrow\uparrow \right\rangle; \quad T_- = \left| \downarrow\downarrow \right\rangle \end{gathered} \qquad \text{(S4)}$$

We use this Singlet-Triplet basis for both the hydride spins (H, H’) as well as for the nitrogen spins (N, N’) and identify all possible combinations resulting in 16 possible states for the system at hand, sorted by their symmetry:

10 symmetric states with respect to exchange of H with H′ and N with N′:

$$\begin{gathered} S_0^H S_0^N,\ T_0^H T_0^N, \\ T_+^H T_-^N,\ T_-^H T_+^N, \\ T_+^H T_+^N,\ T_-^H T_-^N, \\ T_0^H T_+^N,\ T_+^H T_0^N, \\ T_0^H T_-^N,\ T_-^H T_0^N; \end{gathered} \tag{S5a}$$

6 antisymmetric states with respect to exchange of A with A′ and B with B′:

$$\begin{gathered} S_0^H T_0^N,\ T_0^H S_0^N, \\ S_0^H T_+^N,\ T_+^H S_0^N, \\ S_0^H T_-^N,\ T_-^H S_0^N; \end{gathered} \tag{S5b}$$

Once we represent the Hamiltonian of Eq. S3 in the basis introduced in Eqs. S5 we obtain a 16x16 matrix, depicted in its entirety in the Appendix of this supplement. This Hamiltonian can drive hyperpolarization from the hydride singlet, $\mathrm{S}_0^{\mathrm{H}}$, into other states that produce either hyperpolarized $^{15}N_2$- magnetization by affecting populations in the $\mathrm{T}_+^{\mathrm{N}}, \mathrm{T}_-^{\mathrm{N}}$ states or $^{15}N_2$- singlet order by affecting the S_0^N, (T_0^N) populations.

The initial state is the parahydrogen derived singlet on the HH’ hydride pair and all other states have close to zero population. Hence, our initial state has the following populations:

$$\begin{gathered} p(S_0^H S_0^N) = p(S_0^H T_-^N) = p(S_0^H T_0^N) = p(S_0^H T_+^N) = 0.25; \\ p(other\,states) = 0 \end{gathered} \tag{S6}$$

We choose a subset of state combinations from the full Hamiltonian to illustrate how *magnetization* is created at very low fields inside the magnetic shields and *singlet order* at a much wider range of magnetic fields.

2.1 Creating $^{15}N_2$ magnetization at low field in magnetically shielded environments

For example, the state $S_0^H S_0^N$ can be connected to the state $T_+^N T_-^N$:

$$\begin{array}{c} \\ \left|S_0^H S_0^N\right\rangle \\ \left|T_+^H T_-^N\right\rangle \end{array} \begin{array}{c} \begin{array}{cc} \left|S_0^H S_0^N\right\rangle & \qquad\qquad \left|T_+^H T_-^N\right\rangle \end{array} \\ \begin{pmatrix} -J_{HH} - J_{NN} & \dfrac{\Delta J_{far} - \Delta J_{near}}{4} \\ \dfrac{\Delta J_{far} - \Delta J_{near}}{4} & \nu_H - \nu_N - \dfrac{\Sigma J_{far} + \Sigma J_{near}}{4} \end{pmatrix} \end{array} \tag{S7}$$

The connection between the states is established when the difference between the diagonal elements is made small. The off-diagonal element connecting the states can then drive the hyperpolarization from the hydrides S_0^N into the $^{15}N_2$ magnetization state T_-^N .

Accordingly, the resonance condition for creating magnetization is obtained when setting the diagonal elements equal to one another:

$$(\nu_H - \nu_N) = -J_{HH} - J_{NN} + \frac{\Sigma J_{near} + \Sigma J_{far}}{4} \qquad \text{(S8)}$$

Also notice that, according to Eq. S7, nitrogen singlet, S_0^N is depleted and the hydride magnetization, T_+^H , is created, which results in hyperpolarized ortho-hydrogen.

Notice that all resonance conditions that have the potential to create magnetization, *i.e.* those that alter T_+^N, T_-^N population will be dependent on frequency terms as in the two examples above. This feature makes creation of magnetization highly field dependent.

With the resonance conditions of Eq. S8 we can qualitatively predict the experimental results as follows. We solve Eq. S8 to give us the magnetic field at which they are fulfilled by substituting $(\nu_H - \nu_N)$ by $B_0(\gamma_H - \gamma_N)$ and obtain

$$B_0 = \frac{-J_{HH} - J_{NN} + \frac{\Sigma J_{near} + \Sigma J_{far}}{4}}{(\gamma_H - \gamma_N)} \qquad \text{(S9)}$$

We can now input estimates for the *J*-couplings in the system, under the assumption that the average residence time of the substrates on the complex is on the order of 100 ms. This implies that the *J*-couplings are only defined within ±10 Hz.

Using values $J_{HH} \approx -10Hz$, $J_{NN} \approx 20Hz$, $\Sigma J_{near} \approx -5Hz, \Sigma J_{far} \approx 0$, $\gamma_H = 4.2576$ kHz/G, γ_N =-0.4316 kHz/G we obtain a numerical value for the magnetic field at which hyperpolarization is created as $B_0 \cong 6$ mG; this matches our experimental findings. As the *J*-couplings in the system are associated with a large uncertainty it is not surprising that the resonance condition is relatively broad. Other combinations of states in the Hamiltonian, connected by off-diagonal elements, also have the potential to create hyperpolarized magnetization in an analogous fashion.

If magnetization is created on ^{15}N then, because of symmetry conservation, magnetization in the opposite direction also has to be created on hydrogen. Furthermore, hyperpolarized magnetization on ^{15}N implies population differences on T_+^N, T_-^N states and hyperpolarized magnetization implies population differences on T_+^H, T_-^H states. Examination of the full

Hamiltonian reveals that diagonal elements of states containing $\mathrm{T}_+^\mathrm{N},\mathrm{T}_-^\mathrm{N}$ or $\mathrm{T}_+^\mathrm{H},\mathrm{T}_-^\mathrm{H}$ are always dependent on frequencies ν_N and ν_H. Therefore, we can only expect hyperpolarized magnetization to form in the magnetic shields where these frequencies are small and comparable in size to the *J*-couplings, such that energy level matching occurs. As another example take the combination of $\left|S_0^H T_-^N\right\rangle$ and $\left|T_-^H S_0^N\right\rangle$ which can create ^{15}N magnetization by depleting the T_-^N state. Here the matching condition, derived by setting the diagonal elements equal to one another, is:

$$(\nu_H - \nu_N) = J_{HH} - J_{NN} \tag{S10}$$

Assuming that the J_{NH}-terms, ΣJ_{near} and ΣJ_{far} (see Eq. S9), are small compared to the associated uncertainties of ±10 Hz, given the short catalytic lifetimes of ~100 ms, we choose to ignore J_{NH}-terms. With the understanding that the matching conditions are broad relative to the size of the involved *J*-couplings we combine Eq. S9 and S10 to arrive at the generalized matching condition presented in the main manuscript.

$$(\nu_H - \nu_N) = \left|J_{HH} \pm J_{NN}\right| \tag{S11}$$

In forthcoming work we will discuss full spin dynamics simulations governed by the Hamiltonian of Eq. S1 to unravel the hyperpolarization process in full detail.

2.2 Creating $^{15}N_2$ singlet order has a weak field dependence

Generation of singlet order is also predictable using the Hamiltonian introduced in Eqs. S1-S3 and listed in matrix representation in the appendix.

In particular, notice the connection of state $\left|S_0^H S_0^N\right\rangle$ to $\left|T_0^H T_0^N\right\rangle$ and the connection of $\left|S_0^H T_0^N\right\rangle$ to $\left|T_0^H S_0^N\right\rangle$, which appear as follows:

$$\begin{array}{c} \\ \left|S_0^H S_0^N\right\rangle \\ \left|T_0^H T^N\right\rangle \end{array} \begin{array}{c} \begin{array}{cc} \left|S_0^H S_0^N\right\rangle & \left|T_0^H T_0^N\right\rangle \end{array} \\ \begin{pmatrix} -(J_{HH} + J_{NN}) & \dfrac{\Delta J_{near} - \Delta J_{far}}{4} \\ \dfrac{\Delta J_{near} - \Delta J_{far}}{4} & 0 \end{pmatrix} \end{array} \tag{S12}$$

and

$$\begin{array}{ccc} & \left|S_0^H T_0^N\right\rangle & \left|T_0^H S_0^N\right\rangle \\ \left|S_0^H T_0^N\right\rangle & -J_{HH} & \dfrac{\Delta J_{near}-\Delta J_{far}}{4} \\ \left|T_0^H S_0^N\right\rangle & \dfrac{\Delta J_{near}-\Delta J_{far}}{4} & -J_{NN} \end{array} \qquad \text{(S13)}$$

The hydrogen singlet S_0^H is the polarization source, therefore Eq. S12 has the potential to deplete the nitrogen singlet, S_0^N, whereas Eq. S13 has the potential to populate the nitrogen singlet, S_0^N. As in the context of creating magnetization, the off-diagonal elements are most efficient at driving transitions whenever the difference between the on-diagonal elements are comparatively small.

We obtain the resonance conditions by setting the diagonal elements equal to one another:

From Eq. S12 we obtain

$$J_{HH} = -J_{NN} \qquad \text{(S14)}$$

Whereas from Eq. S13 we obtain

$$J_{HH} = J_{NN} \qquad \text{(S15)}$$

We combined these two for the main manuscript and generalize the singlet order producing resonance condition as:

$$J_{HH} = \pm J_{NN} \qquad \text{(S16)}$$

We believe that for the particular system at hand, both $J_{HH}\,(\approx -10Hz)$ and $J_{NN}\,(\approx -20Hz)$ are negative and that it is the connection between $\left|S_0^H T_0^N\right\rangle$ and $\left|T_0^H S_0^N\right\rangle$ that produces hyperpolarized singlet. It is apparent that the resonance condition cannot be matched by changing the magnetic field because *J*-couplings do not depend on the magnetic field and therefore the resonance condition cannot be filled exactly. This also explains why pumping singlet is slightly less efficient than pumping magnetization.

Lastly, the singlet can no longer be populated at magnetic fields at which the model depicted in Fig. S2 is no longer valid. That is, as soon as the frequency difference between the two nitrogens bound to the catalyst becomes larger than the NN *J*-coupling the singlet state is no longer an eigenstate.

3) Spin dynamics during low to high field sample transfer

To enable the detection of the hyperpolarized states we transfer the sample from the low field region where hyperpolarization occurs into the high field magnet for detection.

Note that field cycling is only one of many possibilities to access long lived-singlet states. Other options include specialized pulse sequences or chemical transformations (*13, 44, 62-64*).

The transfer process from low to high field of either magnetization or singlet order is highly adiabatic. This implies that populations will stay on eigenstates of the system during the adiabatic transfer process. In Fig. S3 we plot the eigenstates as a function of magnetic field. At low field the singlet and triplet states are the eigenstates and at high field the usual Zeemann states are the eigenstates.

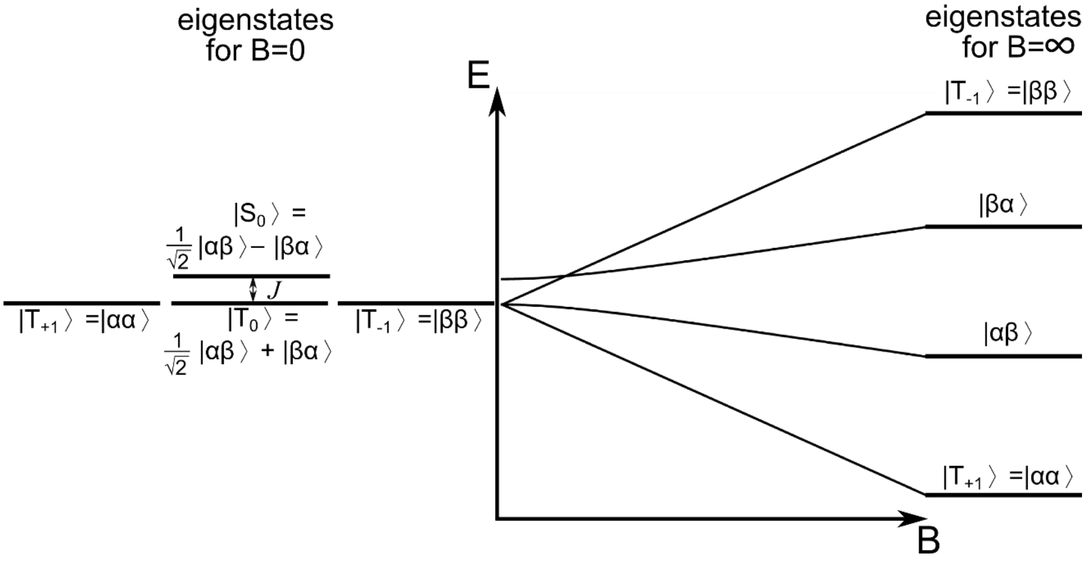

fig. S3. Eigenstates of a *J*-coupled 2-spin system as a function of magnetic field. Initial singlet population is converted in an adiabatic process into pure $|\beta\alpha>$ population because at any moment during the adiabatic transfer the population remains in an eigenstate of the system. The figure shows the scenario for a negative *J*: The singlet is higher in energy than the triplets at zero field.

Magnetization, represented as $I_{1z}+I_{2z}$, is associated with population difference between the $\alpha\alpha$ and $\beta\beta$ states, which are eigenstates at both low and high fields. Therefore, magnetization remains unchanged during the transfer process. When $I_{1z}+I_{2z}$ is probed with a 90° pulse we obtain a simulated spectrum, as displayed in Fig S4A, which matches well with the experimental data.

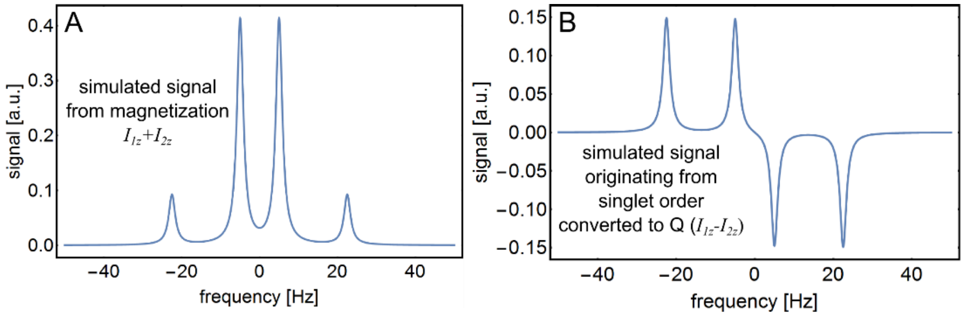

fig S4. **Simulated spectra for magnetization and singlet order.** Simulated spectra for A) signal originating from magnetization ($I_{1z}+I_{2z}$) and B) signal originating from singlet order that is converted into ($I_{1z}-I_{2z}$) upon adiabatic transfer from low field to high field and subsequently detected with 90-acquire. Spinsystem parameters: J_{NN}=-17.5 Hz; $\Delta\nu$ = 21.2 Hz , $Q=\frac{\Delta\nu}{\sqrt{\Delta\nu^2+J_{NN}{}^2}}$ (see Eq. S20).

The singlet order, on the other hand, is only an eigenstate at low magnetic fields and is not directly detectable but it is converted into a detectable state by the transfer from low to high magnetic field if a small chemical shift difference between the two ^{15}N spins is present To enable this transformation, we designed our $^{15}N_2$-diazirine with a chiral center creating the required small chemical shift difference between the two ^{15}N nuclei ($\Delta\delta$=0.58 ppm). At low magnetic fields, i.e. 1 kG and below, ($\Delta\delta \leq 0.3$ Hz) this chemical shift difference is small enough compared to the ^{15}N-^{15}N one bond *J*-coupling (J_{NN}=17.3 Hz) such that singlet order is well protected from coherent evolution and subsequent relaxation (*46*, *62*). Upon transfer to a high magnetic field (i.e. 8.5 T) the symmetry is broken because, the chemical shift difference ($\Delta\delta$(8.5 T)=21 Hz) is now larger than J_{NN} (17.3 Hz) and a detectable state will have emerged producing the observed anti-phase spectral patterns.

The singlet, starts out in the state $\left|\alpha\beta-\beta\alpha\right\rangle/\sqrt{2}$ which is not an eigenstate at high magnetic fields. We calculate the associated eigenstate as a function of magnetic field, or rather the frequency difference between the ^{15}N nuclei, $\Delta\nu$, which is proportional to the magnetic field, and obtain (without normalization):

$$\left|eigenstate(\Delta\nu)\right\rangle=\frac{\sqrt{\Delta\nu^2+J_{NN}{}^2}-\Delta\nu}{J_{NN}}\left|\alpha\beta\right\rangle-\left|\beta\alpha\right\rangle \tag{S17}$$

For $\Delta\nu$ = 0 the normalized eigenstate is the singlet state $|\alpha\beta - \beta\alpha\rangle / \sqrt{2}$ and for $\Delta\nu = \infty$ the eigenstate is $-|\beta\alpha\rangle$.

From this field dependent eigenstate we also calculate the field dependent density matrix as:

$$\rho(\Delta\nu) = |eigenstate(\Delta\nu)\rangle\langle eigenstate(\Delta\nu)| \tag{S18}$$

And we obtain the initial density matrix where $\Delta\nu$ = 0 as

$$\rho_0 = \frac{1}{4}\hat{\mathbf{1}} - (I_{1z}I_{2z} + I_{1x}I_{2x} + I_{1y}I_{2y}) \tag{S19}$$

When raising the field this density matrix develops into:

$$\rho(\Delta\nu) = \frac{1}{4}\hat{\mathbf{1}} - I_{1z}I_{2z} - \frac{J_{NN}}{\sqrt{\Delta\nu^2 + J_{NN}{}^2}}(I_{1x}I_{2x} + I_{1y}I_{2y}) - \frac{\Delta\nu}{\sqrt{\Delta\nu^2 + J_{NN}{}^2}}\frac{1}{2}(I_{1z} - I_{2z})\,. \tag{S20}$$

For infinitely high magnetic field this corresponds to $\frac{1}{4}\hat{\mathbf{1}} - I_zS_z - \frac{1}{2}(I_{1z} - I_{2z})$, which is a pure population of the βα state.

When $\rho(\Delta\nu)$ is probed with a 90° pulse only the I_{1z}-I_{2z} component gives signal resulting in two antiphase doublets as displayed in Fig S4 B) matching the experimentally observed spectra.

4) *Ab initio* characterization of candidate structures enabling spin transfer from p-H_2 to $^{15}N_2$-diazirine

In order to understand the adsorption geometries of possible catalytic species that promote hyperpolarization transfer, we undertook density-functional theory based electronic structure calculations of specific structure candidates involving Diazirine and/or the Ir-containing catalyst. The calculations were performed using the FHI-aims (*40*, *41*) a full-potential, all-electron electronic structure code based on numeric atom-centered orbital basis sets. Importantly, these numerically tabulated basis sets include atomic radial functions that fulfill the nuclear cusp conditions, i.e. provide a natural all-electron description also of heavy elements such as Ir. The detailed nomenclature of basis sets and numerical settings of FHI-aims are described in detail in Ref. (*40*). For the present work, tier 2 basis sets and predefined “tight” integration settings, enabling an essentially numerically and basis-set converged description of the energetics of weakly bonded systems.(*40*, *65-67*) To model the exchange-correlation energy functional, we use the PBE density functional corrected for dispersion interactions following two different approaches: *(i)* initially, the Tkatchenko-Scheffler (PBE+TS) pairwise dispersion correction (*68*) for determination of the configurations of the diazirine substrate as isolated molecule, followed by *(ii)* a recomputation using a recent, more accurate many-body dispersion model, referred to as MBD@rsSCS(*39*) or PBE+MBD* for short. All structures were fully relaxed to local minima of the potential energy surface, with residual total energy gradients below 0.01 eV/Å.

Atomic structure models of different diazirine-containing systems were constructed as follows: We first assembled a list of plausible low-energy candidate conformations of the isolated diazirine molecule (2-cyano-3-(D_3-methyl-$^{15}N_2$-diazirine)-propanoic acid). We then used these candidate conformation to construct adsorbed candidate conformations of the full Diazirine+SABRE catalyst complex in a manual approach. It should be noted that the SABRE catalyst places significant conformational restrictions on how the Diazirine conformations can be attached. These restrictions are the primary reason for the manual approach to conformation construction chosen here.

The key insight related to hyperpolarization transfer that emerges from the full Diazirine+SABRE catalyst conformations is that the Diazirine binding occurs in the theta-1 (over edge) rather than the theta-2 (N2 double bond adsorption) conformation (see description and especially Table S1 below).

Among five local structure minima tested for the isolated diazirine molecule, three conformations emerged as low-energy candidates using the PBE+TS DFT approach, shown in Fig. S5. We named them (Var 1), (Var 2), related to Var1 by a rotation of the carboxyl group and (Var3) related to Var1 by a rotation of the diazirine group. It is worth noting that one of them (Var3) is not a local structure optimum in the PBE+MBD* approach. Since the primary use of Var 3 is the construction of adsorbed candidate geometries with the SABRE catalyst, the PBE+TS structures were used to ensure conformational variety.

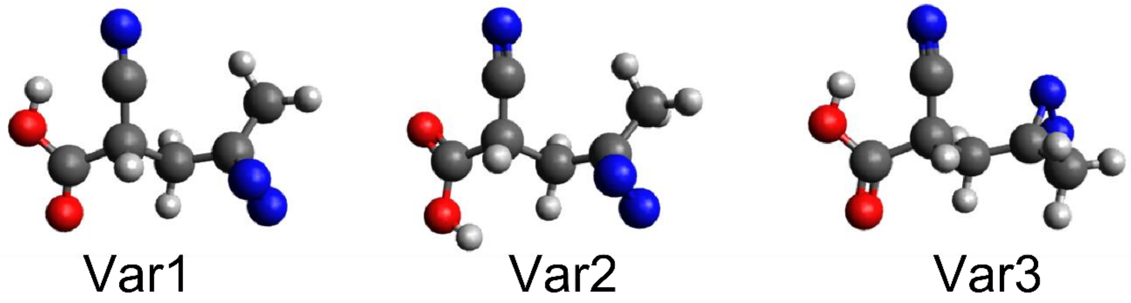

fig. S5. Three candidate conformations of 2-cyano-3-(methyl-$^{15}N_2$-diazirine)-propanoic acid as identified by DFT PBE+TS calculations, as used to construct likely catalytically active structures producing hyperpolarization attached to the SABRE catalyst. Blue: nitrogen, red: oxygen, grey: carbon, white protons. Relative energies calculated by DFT (PBE+TS functional): 0 eV (Var1), 0.176 eV (Var2), 0.037 eV (Var3).

Based on the manually constructed geometries of the Diazirine Var1, Var2 and VAr3 conformers adsorbed at the Iridium catalyst, we identified the four catalytic species depicted in Fig. S5 as the most likely species to play important roles in the presented experiments at different concentrations and temperatures. These are:

- binding of just one diazirine molecule (Fig S6a), when using the [Ir(COD)(IMes)(Py)][PF_6]
- binding of two diazirine molecules, one through the cyano group, the other through the diazirine group (figS6b) when using the [Ir(COD)(IMes)(Py)][PF_6] precursor.
- binding of a pyridine molecule and a diazirine molecule, either through the diazirine group (fig S6c) or the cyano group (Fig S6d) when using the traditional [IrCl(COD)(IMes)] with excess pyridine in solution .

In all cases the axial ligands are IMes and pyridine.

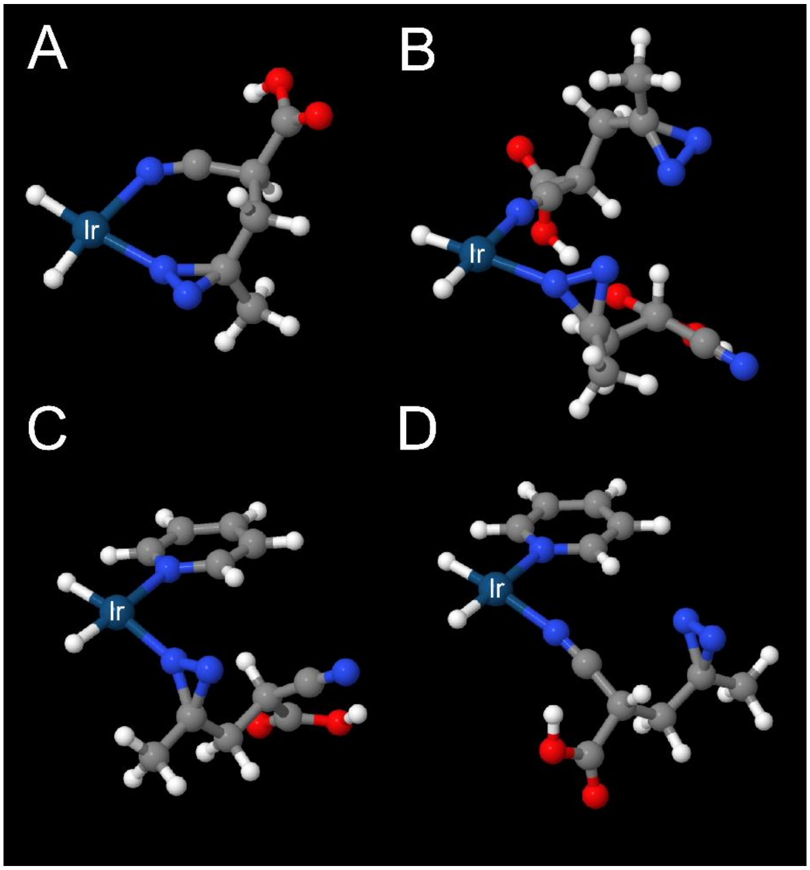

fig. S6. First-principles derived candidate conformations of catalytic species that drive hyperpolarization transfer. (Local minimum-energy structures of the potential energy surface at the level of DFT PBE+MBD* as described in the text). The iridium is always coordinated in an octahedral fashion but the axial ligands, IMes and pyridine, are not shown for clarity. Only the ligands in the equatorial plane are depicted. A) Ir binds two hydrides and the diazirine molecule in a bidentate mode. B) Ir binds two hydrides and two diazirine molecules. One of those binds via the diazirine group itself whereas the other binds through its cyano group. A) and B) are the most likely catalytic species when the [Ir(COD)(IMes)(Py)][PF_6] precursor is used because no extra pyridine was added to the solutions, however if [IrCl(COD)(IMes)] was additional free pyridine was in solution to stabilize the complexes hence structures in C) and D) are more likely.

Detailed results and discussion of various catalytic species and attachment modes:

We initially considered attachments of the diazirine molecule to the Iridium center via the O and N atoms, including binding of the diazirine group via a single nitrogen with its lone-pair (η^1 binding) or via both N atoms (and the shared double bond, η^2 binding). Attachments through the O atoms are highly unfavorable and were quickly abandoned (~ 0.5 eV higher in energy than single sided N-binding). Attachment via the N=N double bond is also energetically unfavorable. (~0.5 eV higher than single sided N-binding, see Table S1). However, binding via the cyano group is comparable in energy to the single-sided diazirine binding.

It is important to note that the precise number of Diazirine ligands attached to the SABRE catalyst vs. competing ligands present in solution will depend on the temperature and respective concentrations of each solute. In order to capture likely adsorption states of the catalyst spanning different conditions, we modeled several structural families.

First, we examined species containing one pyridine and one diazirine molecule attached to the two axial binding sites across the hydrides of the SABRE catalyst and calculated the relative total energies, as compared to the lowest energy structure as given in table S1. Based on the results of Table S1, we concluded that only cyano group attachment and η^1-single-sided diazirine attachment are energetically viable.

Table S1. Relative energies of the diazirine attachment modes tested in this work, for the case of two different ligands that are simultaneously present: two equatorial hydrides, axial IMes, axial pyridine, one equatorial pyridine and diazirine in an equatorial position. All units are eV. Method: DFT PBE+MBD*

Diazirine Configuration	η^2-N=N attachment	η^1-Single-Sided N attachment	Cyano Group Attachment	O Attachment	OH Attachment
Var 1	0.669	0.137 (Fig S6C)	0 (Fig S6D)	0.629	0.742
Var 2	0.845	0.246	0.182	0.651	0.742
Var 3	0.802	0.342	0.099	1.970	0.829

Next, we considered species containing two diazirine molecules in the axial positions and calculated the relative total energies, as compared to the lowest energy structure. The results are given in Table S2. Each column corresponds to a different combination of attachments for the two diazirine molecules. The indicated diazirine configuration is used for both diazirine molecules. We indicated the structure corresponding to the species shown in Fig S6.

Table S2. Relative energies of the diazirine attachment modes tested in this work for the case of two diazirine molecules that are simultaneously present. The ligands are: two equatorial hydrides, axial IMes, axial pyridine, two equatorial diazirine molecules (in plane with the hydrides). All units are eV. Method: DFT PBE+MBD*

Diazirine Configuration	η^1-Single-Sided N attachment for both	η^1-Single-Sided N and Cyano Group Attachment	Cyano Group attachment for both
Var 1	0.236	0.078	0.188
Var 2	0.236	0 (fig S6b)	0.450
Var 3	0.453	0.083	0.014

Lastly, we considered the attachment of a single diazirine to both binding sites of the Ir complex which binds through the cyano group as well as through the diazirine group. We found that only the Var2 configuration could be successfully attached (Fig. S6a).

5) Sample preparation, and experimental setup to obtain well controlled mG fields.

5.1 Sample preparation:

5.1a) Samples hyperpolarized with [Ir(COD)(IMes)(Py)][PF$_6$]

We prepared a stock solution of 0.5 M [Ir(COD)(IMes)(Py)][PF$_6$] in CD$_3$OD. Subsequently, an appropriate aliquot of this stock solution was added into the NMR tube containing CD$_3$OD such that a volume of 600 μL of the targeted concentration was obtained. To this solution we then added an aliquot of a 700 mM solution of the diazirine (**6**) in D$_2$O to achieve the desired diazirine concentration.

5.1b) Samples hyperpolarized with [Ir(COD)(IMes)Cl]

We prepared a stock solution of 0.5 M [Ir(COD)(IMes)Cl] plus 8 equivalents of pyridine i.e. 4 M in CD$_3$OD. Subsequently, an appropriate aliquot of this stock solution was added into the NMR tube containing CD$_3$OD such that a volume of 600 μL at the targeted concentration was obtained. To this solution we then added an aliquot of a 700 mM solution of the diazirine (**6**) in D$_2$O to achieve the desired diazirine concentration.

5.1c) Parahydrogen production

Parahydrogen (*p*-H$_2$) gas (~92% para-state, 8.2 atm) was created in a Bruker® Parahydrogen Generator (BPHG, slightly modified to access higher pressures) and bubbled through the solution prepared above. For catalyst activation the bubbling was performed for 20 min before starting any experiments.

5.2 Experimental setup to obtain well controlled mG fields

A set of three layers of magnetic shielding is used to obtain a low magnetic field environment. (MuMETAL® Zero Gauss Chambers; product #ZG-206, Magnetic Shield Corp.) The shields are degaussed with a degaussing coil (not visible) wrapped around the innermost shield. In the center of the shields we place a solenoid with length L=47.5 cm and N=165 turns (see Fig. S7). Therein we estimate the field, B, as:

$$B = \mu_0 \frac{N}{L} I \,, \tag{S21}$$

where μ_0 is the permeability and I is the current through the coil.

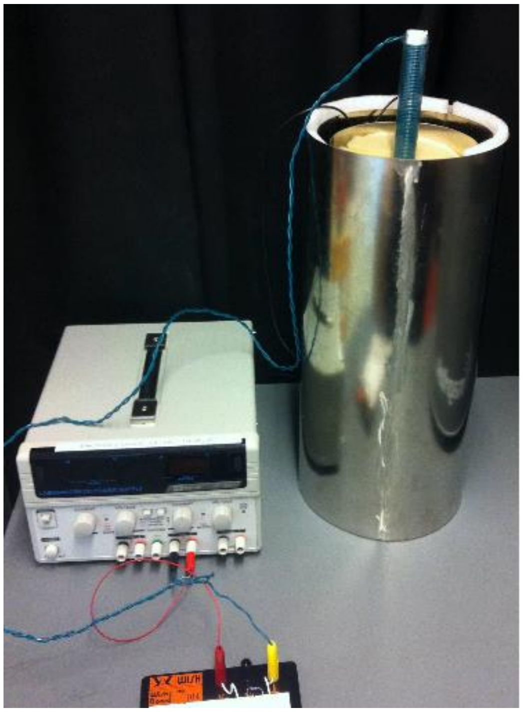

fig. S7. Experimental SABRE-SHEATH setup. Three layers of magnetic shielding (right) provide an environment with residual magnetic fields < 0.5 mG. Fields between 0.5 mG and 130 mG are established by passing a small current through a solenoid within the shields. The current is set by adjusting the voltage (0-30 V) over fixed resistors (typically 1-15 kΩ).

6) Hyperpolarization buildup dynamics, lifetimes and enhancements in detail

In Fig. S8 we summarize our data under various conditions in terms of concentrations and magnetic fields and show the observed effects on A) hyperpolarization lifetime, B) hyperpolarization buildup and C) observed enhancements. These measurements are detailed below.

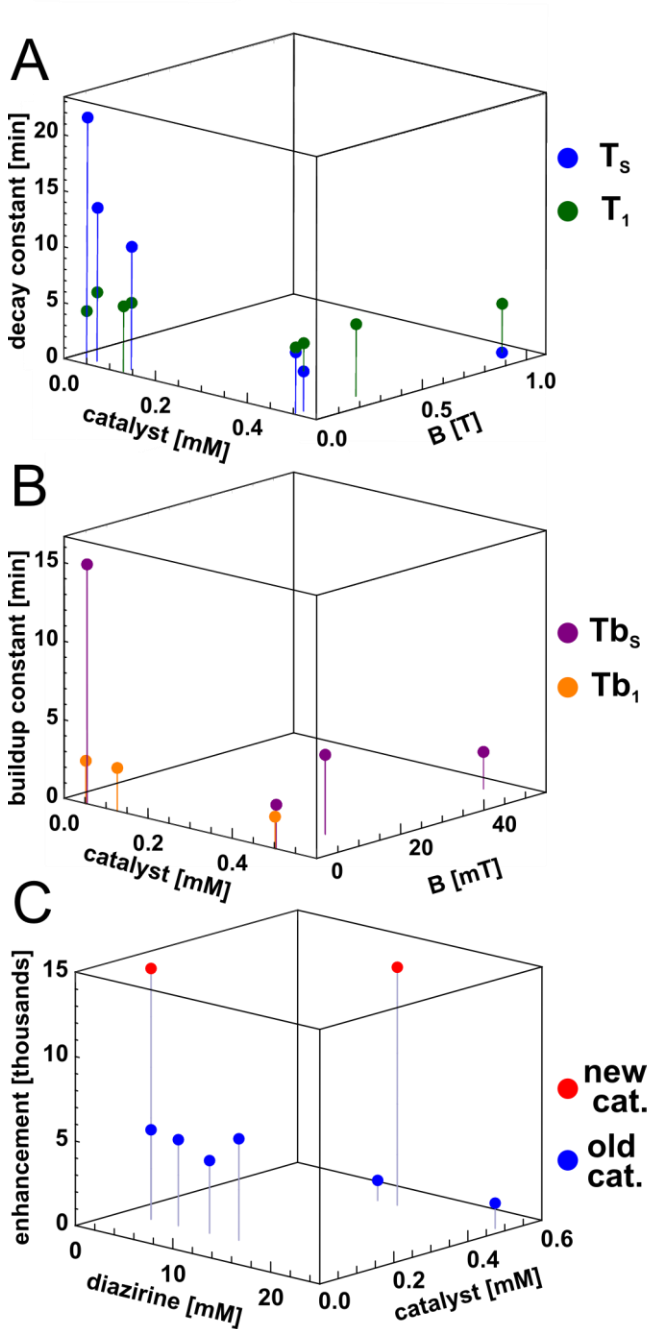

fig. S8. Decay time constants, buildup constants and enhancements as function of magnetic field and concentrations. The effects of varying concentrations and magnetic fields on A) signal decay time constants T_1 and T_S, B) hyperpolarization buildup constants Tb_1 and Tb_S, and C) observed enhancements.

6.1 T_1 measurements

T_1 was measured as a function of catalyst concentration, and holding magnetic field. Magnetization was developed within the magnetic shield at ~6 mG, *para*-H_2 bubbling was stopped and the sample was removed to a specified magnetic field for a variable period of time. The sample was then transported into an 8.5 T spectrometer and the spectrum was immediately recorded with a 90° pulse-acquire. Triplet magnetization signal was deconvoluted from singlet signal, and fitted to a single exponential decay. Data are given in Table S3 and displayed in Fig S8A.

Table S3. Magnetization lifetimes, T_1, under varying catalyst concentration and holding field. [Ir(COD)(IMes)Cl] **(1),** diazirine substrate **(2),** pyridine **(3)**, D_2O, **(4)**
*data displayed in the main manuscript.

[**1**] / mM	[**2**] / mM	[**3**] / mM	[**4**] / mM	B_{hold} / G	T_1 / s
0.05	12	0.4	960	3	282
0.05	12	0.4	960	10000	270
0.05	12	0.4	960	500	367
*0.125	12	1	960	120	348
0.125	12	1	960	500	355
0.5	12	4	960	120	350
0.5	12	4	960	500	361
0.5	12	4	960	3000	384
0.5	12	4	960	10000	274

6.2 Singlet lifetime (T_S) measurements

Singlet lifetime T_S was measured as a function of catalyst concentration, and holding magnetic field. The singlet was hyperpolarized at 3 G, *para*-H_2 bubbling was stopped *and the system was depressurized* before transferring to the holding magnetic field for a variable period of time. The sample was then transported to an 8.5 T spectrometer and the spectrum was immediately recorded with a 90° pulse-acquire. Singlet signal was deconvoluted from any residual triplet magnetization, and fitted to a single exponential decay. At low catalyst concentrations, dissolved *para*-H_2 continued to hyperpolarize the diazirine singlet for up to 5 minutes at a given holding field, and so the first 5 minutes are excluded from the fitted data. A typical dataset illustrating this effect is given in Fig. S9. Note that magnetization does not experience this complication because magnetization is not created at holding fields outside the shields. The resulting data is given in table S4 and plotted in Fig. S8A.

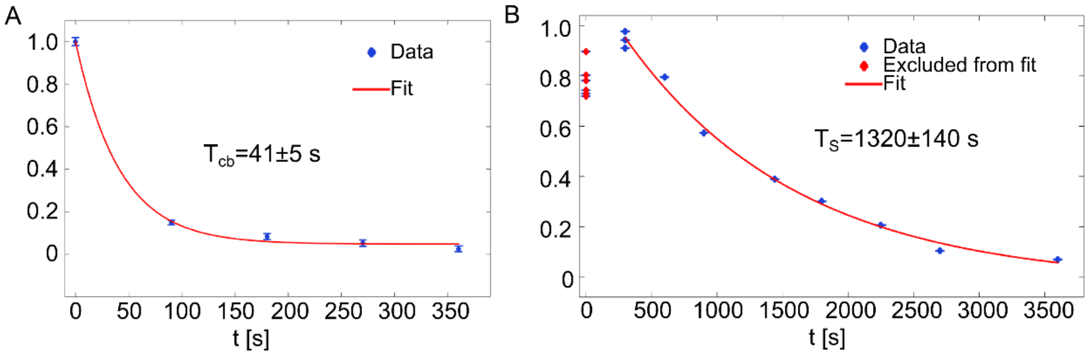

fig. S9. The effect of continued singlet-polarization buildup after stopping *p*-H_2 bubbling. A) the fractional continued build-up, after parahydrogen bubbling is stopped, observed at a holding field of 500 G. After an initial pulse-acquire (at 0 s) a cycle of; leaving the sample in the high-field for 30s (to eliminate residual magnetization), followed by 500 G for 60 s, and another acquisition, was repeated. Initially this continued build-up can be significant – up to 15% of the initial signal. However, by 5 minutes the continued build-up is entirely negligible. The exponential decay constant for continued buildup, T_{cb} is about 41s. B) Typical singlet decay curve. There is an initial continued build-up of signal. To obtain an accurate singlet lifetime only time points after 5 min are fit to an exponential decay. The 5 min exclusion time was chosen based on the observations described in part A. For this particular dataset a singlet lifetime of 22 min is observed.

Table S4. Singlet lifetimes, T_S, under varying catalyst concentration and holding field. [Ir(COD)(IMes)Cl] **(1),** diazirine substrate **(2),** pyridine **(3)**, D_2O, **(4)**
*data displayed in the main manuscript

[**1**] / mM	[**2**] / mM	[**3**] / mM	[**4**] / mM	B_{hold} / G	T_S / s
*0.05	12	0.4	960	3	1320
0.05	12	0.4	960	500	820
0.125	12	1	960	500	655
0.5	12	4	960	120	325
0.5	12	4	960	500	210
0.5	12	4	960	10,000	12

6.3 Tb_1 measurements

Magnetization buildup times, Tb_1, were measured as a function of catalyst concentration. The holding field was kept constant at 6 mG. Magnetization was developed for varying amounts of time and subsequently transported into an 8.5 T spectrometer and the spectrum was immediately recorded with a 90° pulse-acquire. Triplet magnetization signal was deconvoluted from singlet signal, and fitted to a single exponential buildup curve. Data are given in Table S5 and plotted in Fig. S8B.

Table S5. Magnetization buildup times, Tb_1, at 6 mG under varying catalyst concentration. [Ir(COD)(IMes)Cl] **(1),** diazirine substrate **(2),** pyridine **(3)** and D_2O **(4).**
* data plotted in Fig. 3 main manuscript.

[**1**] / mM	[**2**] / mM	[**3**] / mM	[**4**] / mM	B_{hold} / G	Tb_1 / s
0.05	12	0.4	960	0.006	163
0.125	3	1	240	0.006	164
*0.5	12	4	960	0.006	121

6.4 Tb_S measurements

Singlet buildup times, Tb_S, were measured as a function of catalyst concentration and polarization field. Singlet order was developed for varying amounts of time and subsequently transported into an 8.5 T spectrometer and the spectrum was immediately recorded with a 90° pulse-acquire. Singlet signal was deconvoluted from triplet signal, and fitted to a single exponential buildup curve. Data are given in Table S6 and plotted in Fig. S8B.

Table S6. Singlet buildup times, Tb_S, under varying catalyst concentration and magnetic fields. [Ir(COD)(IMes)Cl] **(1),** diazirine **(2),** pyridine **(3)**, D_2O, **(4)**
* data plotted in Fig. 3 main manuscript

[**1**] / mM	[**2**] / mM	[**3**] / mM	[**4**] / mM	B_{hold} / G	Tb_S / s
0.05	12	0.4	960	3	912
0.5	12	4	960	3	165
*0.5	12	4	960	120	302
0.5	12	4	960	500	140

6.5 enhancements measurements

Magnetization enhancements were measured as a function of varying catalyst and substrate (i.e. diazirine) concentrations. The enhancements are obtained by comparison to eight averages of a thermal pulse acquire measurement of a 700 mM sample with 2.03 times larger volume in the active region. Accordingly the enhancements were calculated as:

$$\varepsilon = 2.03 \times 8 \times \frac{700\,\mathrm{mM}}{c(\mathrm{Diaz})} \times \frac{\int hyperpolarized\ signal}{\int thermal\ reference} \qquad \text{(S22)}$$

The measurements were performed with two precursors: [IrCl(COD)(IMes)] and [Ir(COD)(IMes)(Py)][PF_6], giving the enhancements listed in Table S7. The table also provides the associated polarization levels which are calculated from the enhancement as:

$$p_{hyp} = \varepsilon \times p_{therm} = \varepsilon \times tanh\left(\frac{\gamma_{15N}\, B_0}{2k_B T}\right) = \varepsilon \times 2.954 \times 10^{-6} \tag{S23}$$

where $\gamma_{15N} = 4.316\,\text{MHz}/\text{T}$, $B_0 = 8.5\,\text{T}$, $T = 298\,\text{K}$ and $k_B = 20{,}836.6\,\text{MHz}/\text{K}$

Table S7. Enhancements, ε, under varying concentrations of catalyst [IrCl(COD)(IMes)] **(1a),** [Ir(COD)(IMes)(Py)][PF_6] **(1b),** diazirine substrate **(2)**, pyridine (**3**) and D_2O (**4**)
*displayed data in the main manuscript.

[1a]/ mM	**[1b]**/ mM	**[2]** / mM	**[3]**/ mM	[**4**]/ mM	ε	*p* / %
--	0.5	14	0	1120	14,100	4.2
*--	0.125	3	0	240	14,900	4.4
0.5	--	24	2	1920	1,500	0.44
0.5	--	12	2	960	1,200	0.35
0.125	--	12	0.5	960	6,100	1.8
0.125	--	3	0.5	240	5,300	1.6
0.125	--	6	0.5	480	5,100	1.5
0.125	--	9	0.5	720	4,300	1.2

Note, observed singlet signals are typically about 1/3 of the observed magnetization signals. In part, that is because singlet readout is incomplete as described by Eq. S20.

The largest enhancement levels were achieved with [Ir(COD)(IMes)(Py)][PF_6] which produces [Ir(IMes)(H_2)(Py)(Diaz)]$^+$ species (see Fig .1 main manuscript). Upon activation by bubbling hydrogen through the solution. In contrast, when using the traditional [IrCl(COD)(IMes)] precursor (*21*) we used a small amount of pyridine to stabilize the complex during activation. In this case, [Ir(IMes)(H_2)(Py_3)]$^+$ is formed first and diazirine may be added to the solution subsequently. With this latter approach, diazirine has to compete with pyridine for binding sites, which reduces the enhancement levels. With the introduced [Ir(COD)(IMes)(Py)][PF_6] precursor competitive pyridine binding is avoided. We point out that this alternate precursor strategy can be employed for an arbitrary amount of other substrates to avoid competitive pyridine binding, beyond diazirines.

Appendix

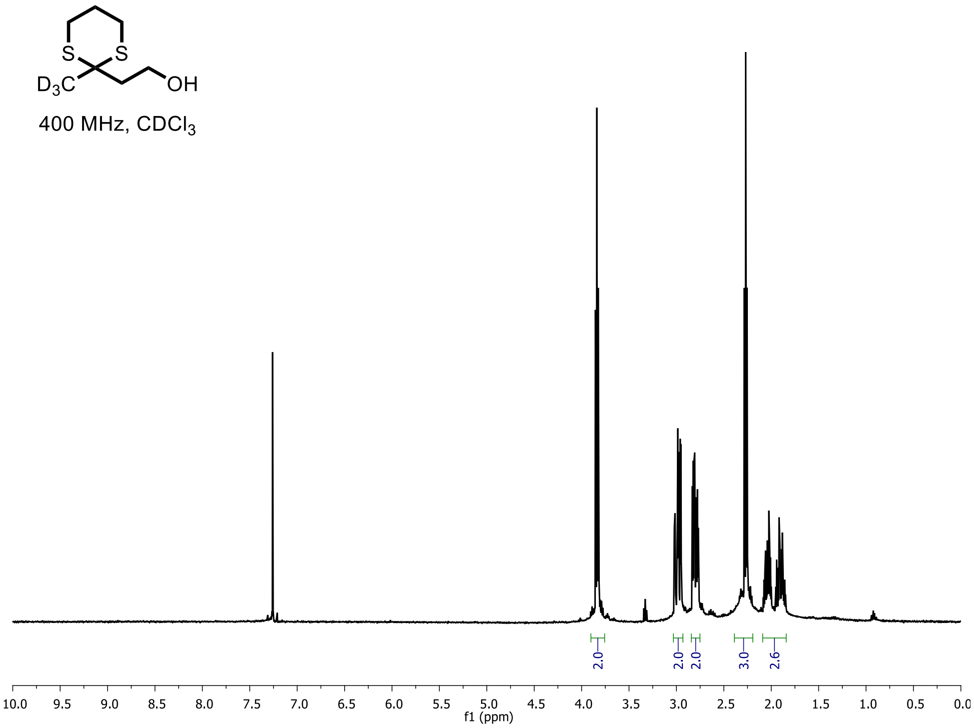

fig. S10 ^{1}H-NMR spectrum of 2-(2’-(Methyl-*d*$_3$)-1’,3’-dithian-2’-yl)ethan-1-ol

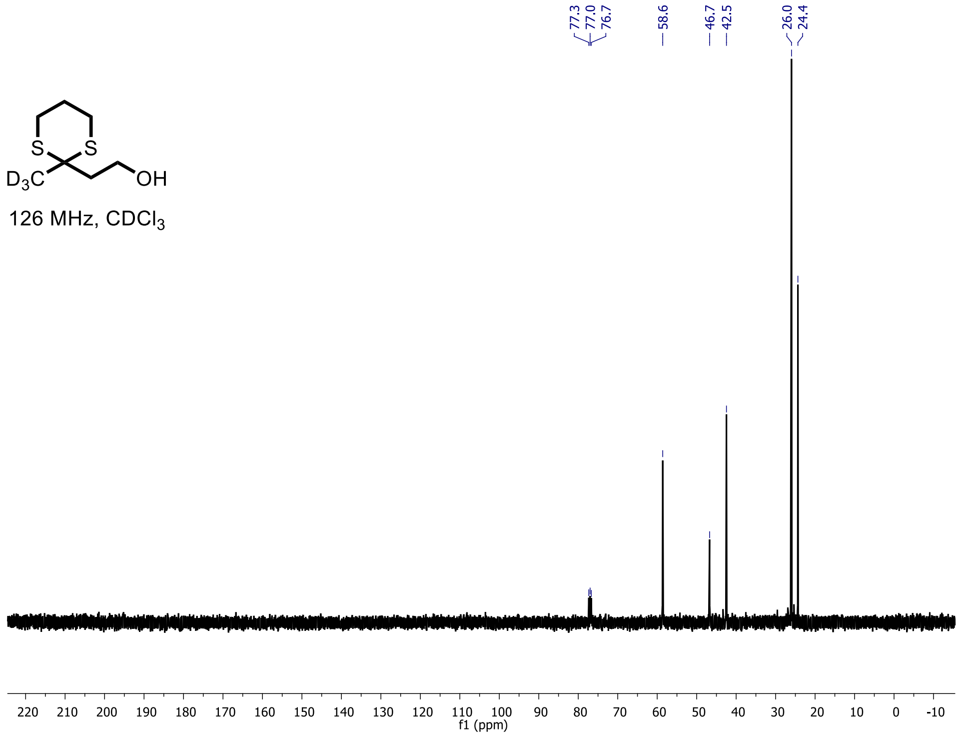

fig. S11 ^{13}C-NMR spectrum of 2-(2’-(Methyl-*d*$_3$)-1’,3’-dithian-2’-yl)ethan-1-ol

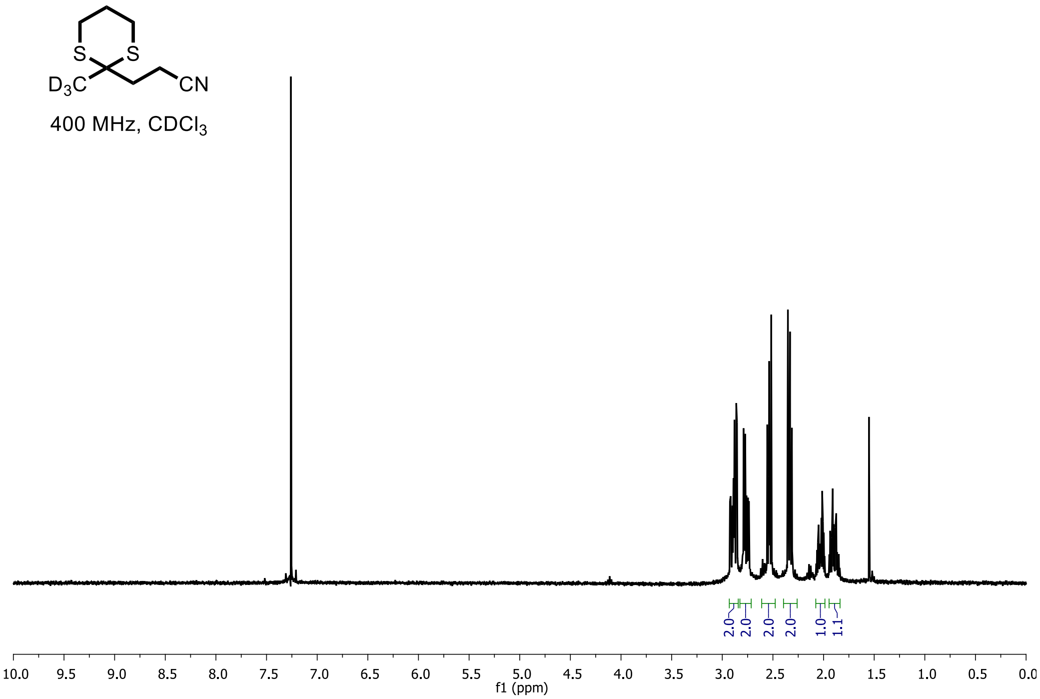

fig. S12. ^{1}H-NMR spectrum of 3-(2’-(Methyl-*d*3)-1’,3’-dithian-2’-yl)propanenitrile

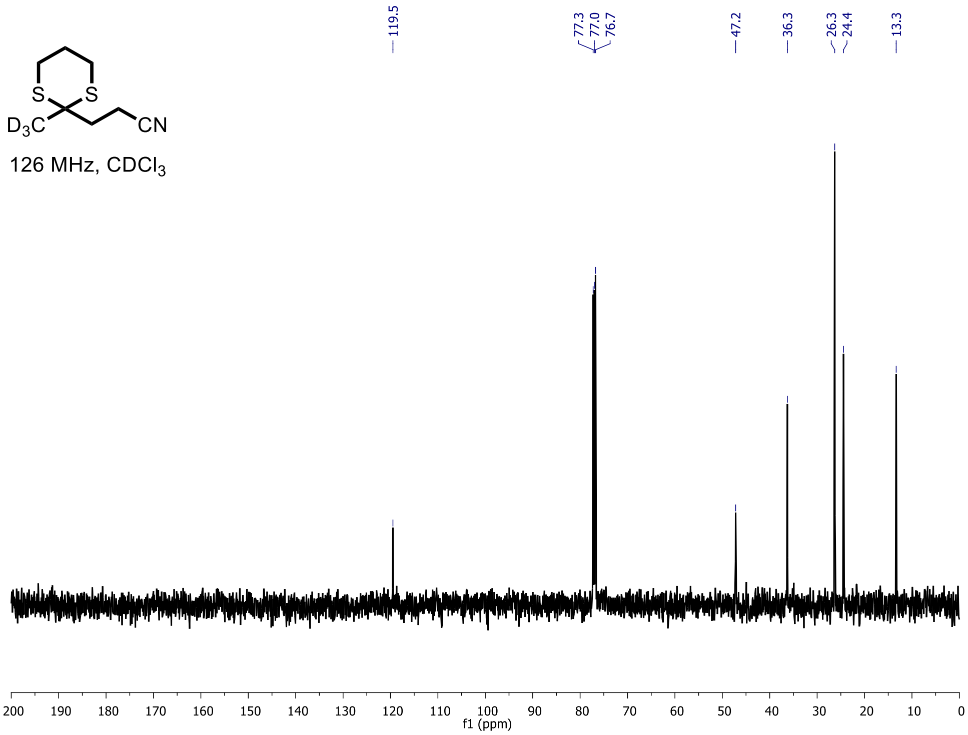

fig. S13. ^{13}C-NMR spectrum of 3-(2’-(Methyl-*d*3)-1’,3’-dithian-2’-yl)propanenitrile

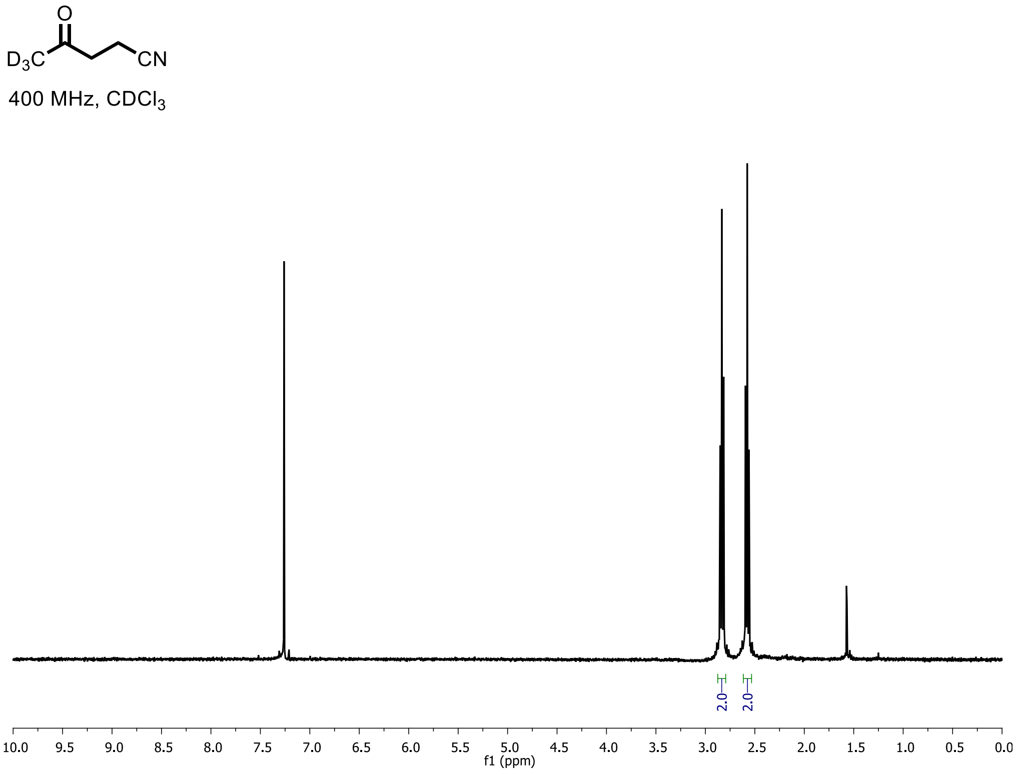

fig. S14 ^{1}H-NMR spectrum of 4-Oxopentanenitrile-5,5,5-d_3

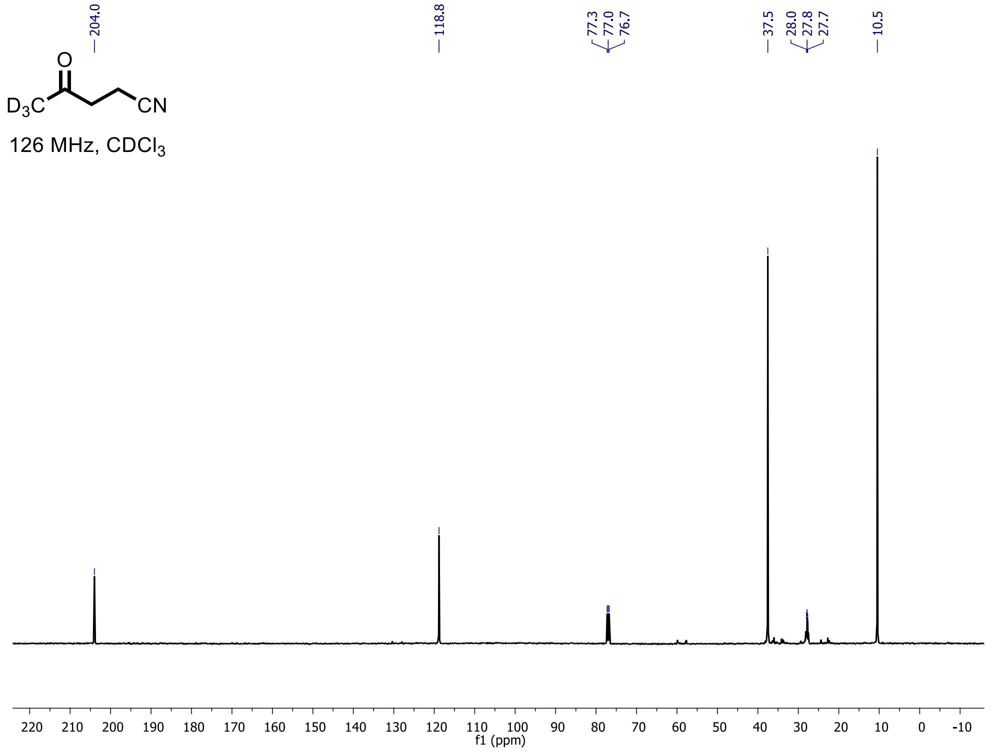

fig. S15 ^{13}C-NMR spectrum of 4-Oxopentanenitrile-5,5,5-d_3

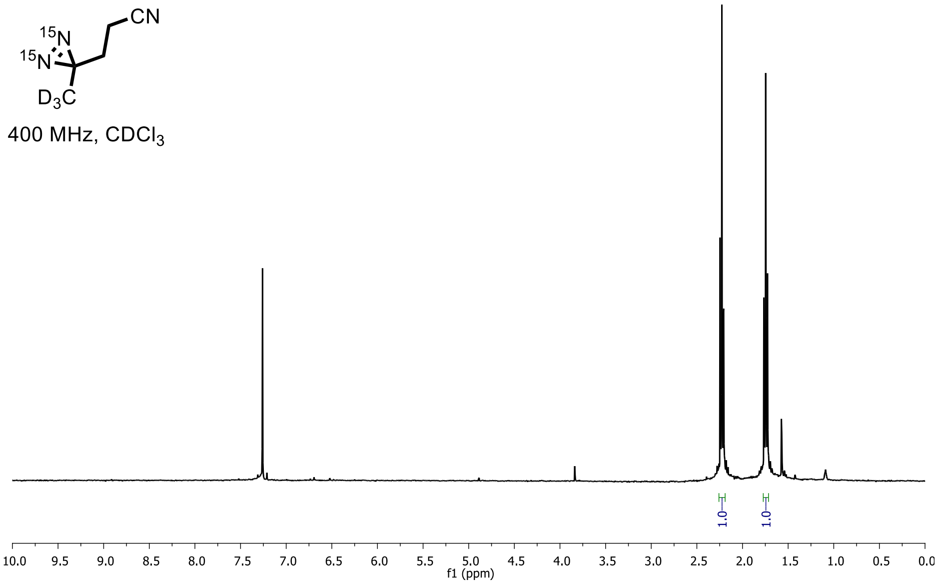

fig. S16 ^{1}H-NMR spectrum of 3-(3’-(Methyl-*d*$_3$)-3’*H*-diazirine-3’-yl-1’,2’-^{15}*N*$_2$) propanenitrile

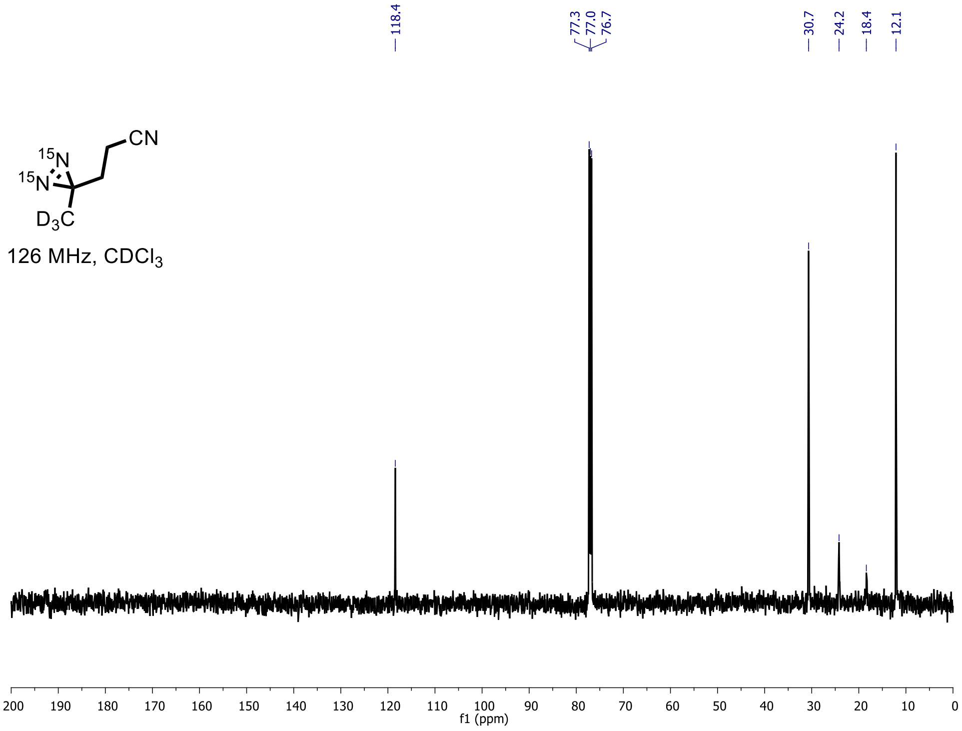

fig. S17 ^{13}C-NMR spectrum of 3-(3’-(Methyl-*d*$_3$)-3’*H*-diazirine-3’-yl-1’,2’-^{15}*N*$_2$) propanenitrile

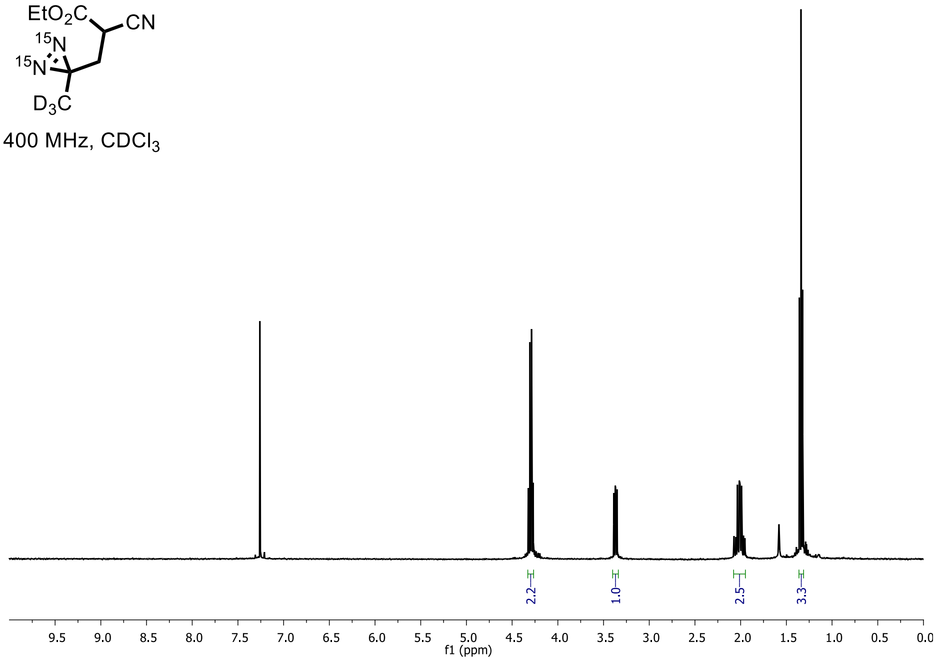

fig. S18 ^{1}H-NMR spectrum of Ethyl 2-cyano-3-(3’-(methyl-d_3)-3’H-diazirine-3’-yl-1’,2’-$^{15}N_2$) propanoate.

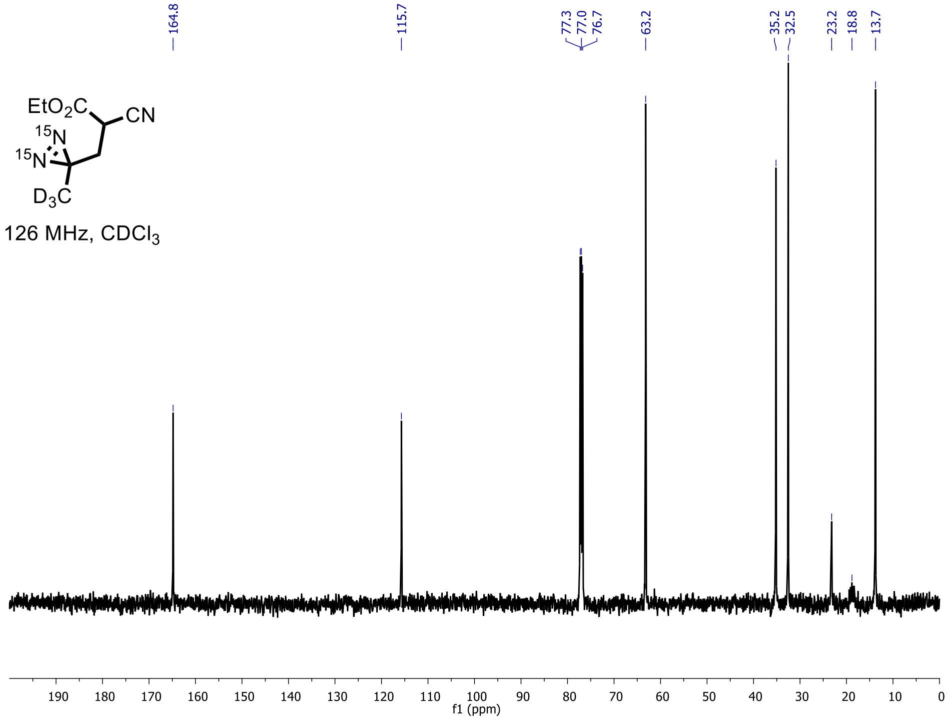

fig. S19 ^{13}C-NMR spectrum of Ethyl 2-cyano-3-(3’-(methyl-d_3)-3’H-diazirine-3’-yl-1’,2’-$^{15}N_2$) propanoate.

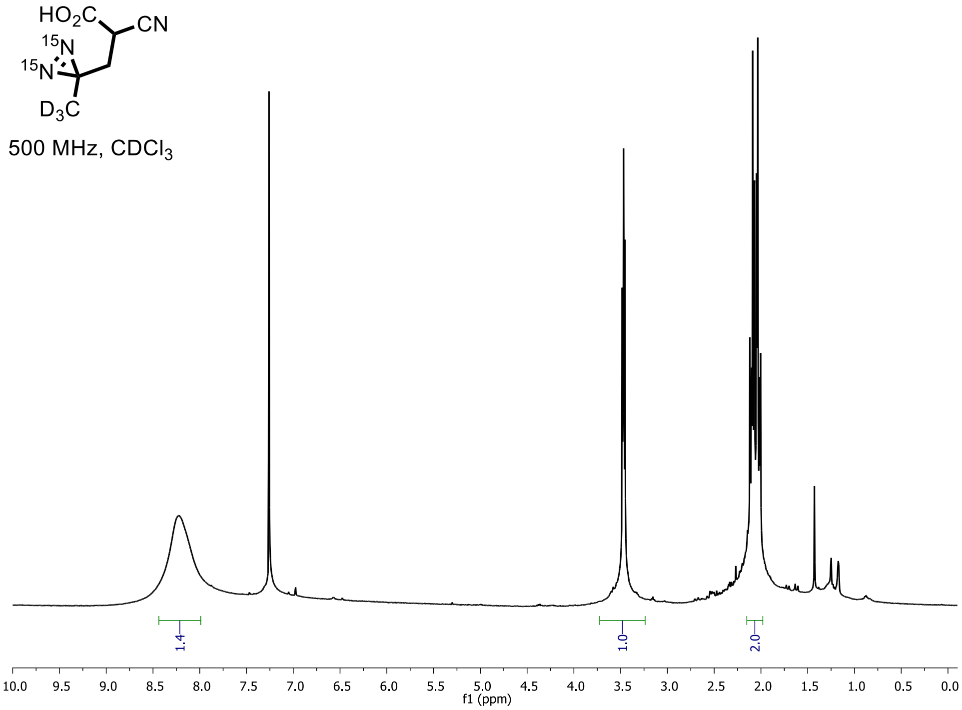

fig. S20 ^{1}H NMR spectrum of 2-Cyano-3-(3’-(methyl-*d*$_3$)-3’*H*-diazirine-3’-yl-1’,2’-^{15}*N*$_2$)propanoic acid

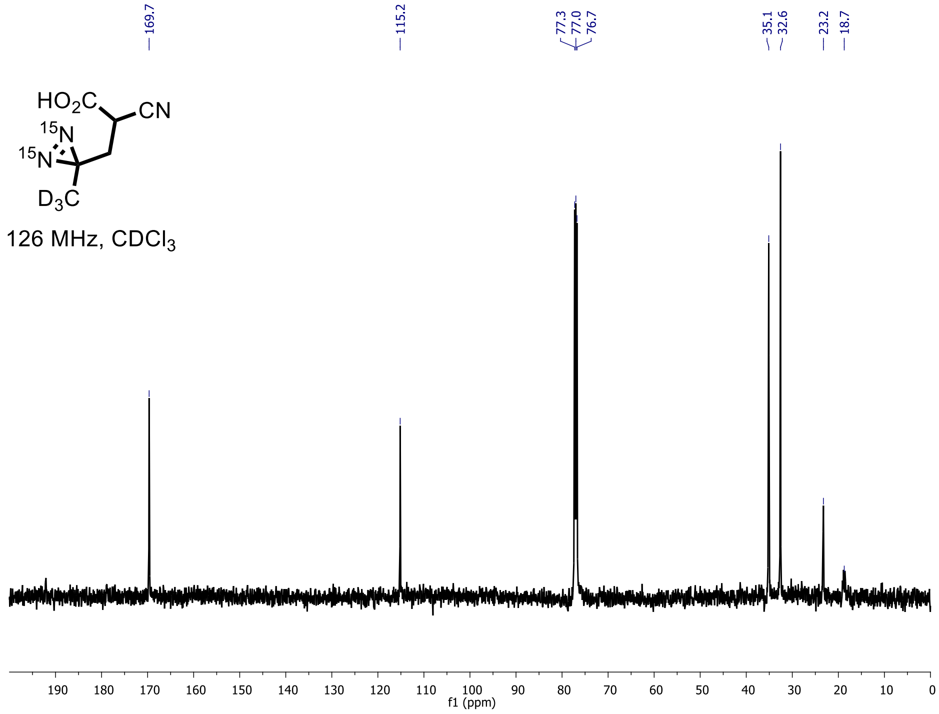

fig. S21 ^{13}C NMR spectrum of 2-Cyano-3-(3’-(methyl-*d*$_3$)-3’*H*-diazirine-3’-yl-1’,2’-^{15}*N*$_2$)propanoic acid

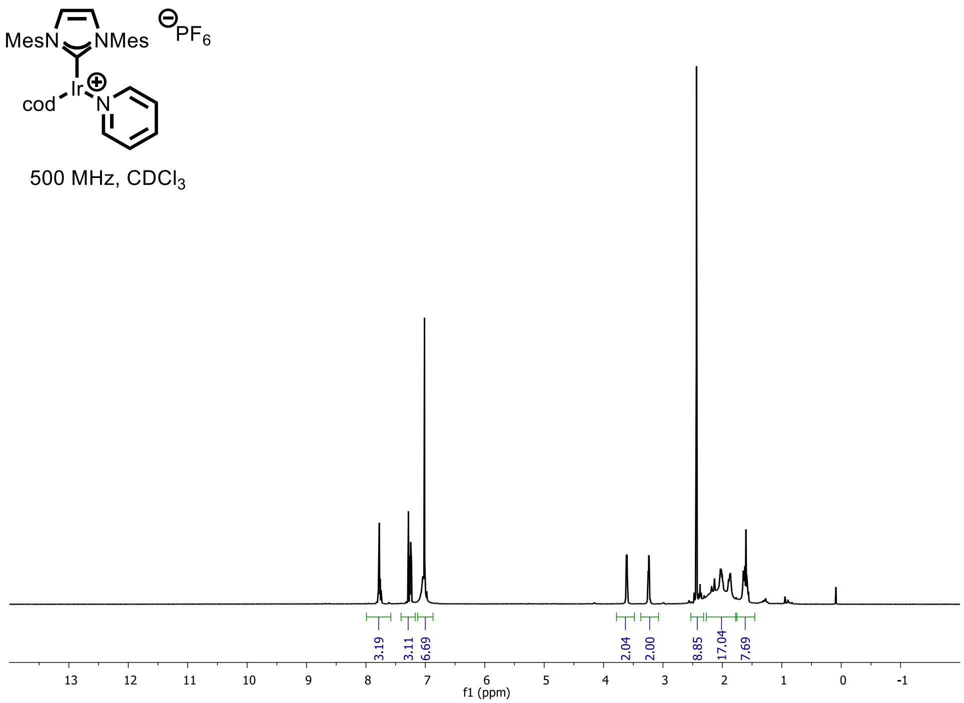

fig. S22 ^{1}H NMR spectrum of (1,5-Cyclooctadiene)(pyridine)(1,3-(2,4,6-trimethylphenyl) imidazol-2-ylidene)iridium(I) hexafluorophosphate.

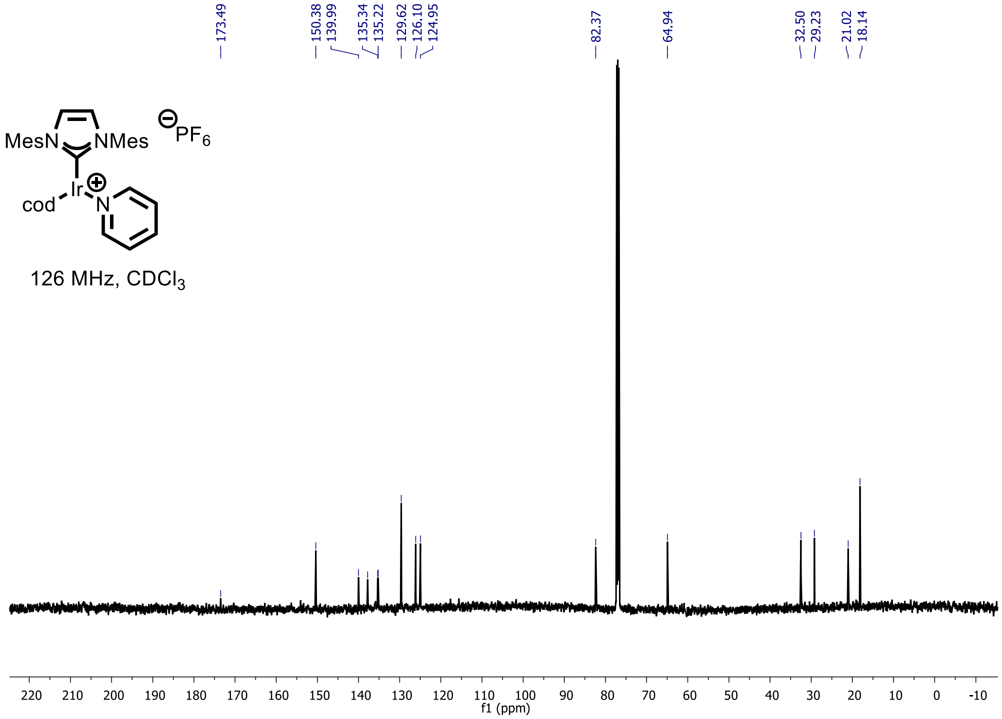

fig. S23 ^{13}C NMR spectrum of (1,5-Cyclooctadiene)(pyridine)(1,3-(2,4,6-trimethylphenyl) imidazol-2-ylidene)iridium(I) hexafluorophosphate.

Hamiltonian from Eq. S1 in the singlet-triplet basis. The blue line indicates the diagonal

$$
\begin{array}{c|cccccccc}
 & \left|S_0^H S_0^N\right\rangle & \left|T_0^H T_0^N\right\rangle & \left|T_+^H T_-^N\right\rangle & \left|T_-^H T_+^N\right\rangle & \left|T_+^H T_+^N\right\rangle & \left|T_-^H T_-^N\right\rangle & \left|T_0^H T_+^N\right\rangle & \left|T_+^H T_0^N\right\rangle \\
\hline
\left|S_0^H S_0^N\right\rangle & -(J_{HH}+J_{NN}) & \frac{\Delta J_{near}-\Delta J_{far}}{4} & \frac{\Delta J_{far}-\Delta J_{near}}{4} & \frac{\Delta J_{far}-\Delta J_{near}}{4} & 0 & 0 & 0 & 0 \\
\left|T_0^H T_0^N\right\rangle & \frac{\Delta J_{near}-\Delta J_{far}}{4} & 0 & \frac{\Sigma J_{near}+\Sigma J_{far}}{4} & \frac{\Sigma J_{near}+\Sigma J_{far}}{4} & 0 & 0 & 0 & 0 \\
\left|T_+^H T_-^N\right\rangle & \frac{\Delta J_{far}-\Delta J_{near}}{4} & \frac{\Sigma J_{near}+\Sigma J_{far}}{4} & (\nu_H-\nu_N)-\frac{\Sigma J_{near}+\Sigma J_{far}}{4} & 0 & 0 & 0 & 0 & 0 \\
\left|T_-^H T_+^N\right\rangle & \frac{\Delta J_{far}-\Delta J_{near}}{4} & \frac{\Sigma J_{near}+\Sigma J_{far}}{4} & 0 & (\nu_N-\nu_H)+\frac{\Sigma J_{near}+\Sigma J_{far}}{4} & 0 & 0 & 0 & 0 \\
\left|T_+^H T_+^N\right\rangle & 0 & 0 & 0 & 0 & \frac{\Sigma J_{near}+\Sigma J_{far}}{4}+\nu_H+\nu_N & 0 & 0 & 0 \\
\left|T_-^H T_-^N\right\rangle & 0 & 0 & 0 & 0 & 0 & \frac{\Sigma J_{near}+\Sigma J_{far}}{4}-(\nu_H+\nu_N) & 0 & 0 \\
\left|T_0^H T_+^N\right\rangle & 0 & 0 & 0 & 0 & 0 & 0 & \nu_N & \frac{\Sigma J_{near}+\Sigma J_{far}}{4} \\
\left|T_+^H T_0^N\right\rangle & 0 & 0 & 0 & 0 & 0 & 0 & \frac{\Sigma J_{near}+\Sigma J_{far}}{4} & \nu_H \\
\left|T_0^H T_-^N\right\rangle & 0 & 0 & 0 & 0 & 0 & 0 & 0 & 0 \\
\left|T_-^H T_0^N\right\rangle & 0 & 0 & 0 & 0 & 0 & 0 & 0 & 0 \\
\left|S_0^H T_0^N\right\rangle & 0 & 0 & \frac{\Delta J_{far}+\Delta J_{near}}{4} & \frac{-\Delta J_{far}-\Delta J_{near}}{4} & 0 & 0 & 0 & 0 \\
\left|T_0^H S_0^N\right\rangle & 0 & 0 & \frac{\Sigma J_{far}-\Sigma J_{near}}{4} & \frac{\Sigma J_{near}-\Sigma J_{far}}{4} & 0 & 0 & 0 & 0 \\
\left|S_0^H T_+^N\right\rangle & 0 & 0 & 0 & 0 & 0 & 0 & \frac{-\Delta J_{far}-\Delta J_{near}}{4} & \frac{\Delta J_{far}+\Delta J_{near}}{4} \\
\left|T_+^H S_0^N\right\rangle & 0 & 0 & 0 & 0 & 0 & 0 & \frac{\Sigma J_{near}-\Sigma J_{far}}{4} & \frac{\Sigma J_{far}-\Sigma J_{near}}{4} \\
\left|S_0^H T_-^N\right\rangle & 0 & 0 & 0 & 0 & 0 & 0 & 0 & 0 \\
\left|T_-^H S_0^N\right\rangle & 0 & 0 & 0 & 0 & 0 & 0 & 0 & 0
\end{array}
$$

$$
\begin{array}{c|cccccccc}
 & \left|T_0^H T_-^N\right\rangle & \left|T_-^H T_0^N\right\rangle & \left|S_0^H T_0^N\right\rangle & \left|T_0^H S_0^N\right\rangle & \left|S_0^H T_+^N\right\rangle & \left|T_+^H S_0^N\right\rangle & \left|S_0^H T_-^N\right\rangle & \left|T_-^H S_0^N\right\rangle \\
\hline
\left|S_0^H S_0^N\right\rangle & 0 & 0 & 0 & 0 & 0 & 0 & 0 & 0 \\
\left|T_0^H T_0^N\right\rangle & 0 & 0 & 0 & 0 & 0 & 0 & 0 & 0 \\
\left|T_+^H T_-^N\right\rangle & 0 & 0 & \frac{\Delta J_{far}+\Delta J_{near}}{4} & \frac{\Sigma J_{far}-\Sigma J_{near}}{4} & 0 & 0 & 0 & 0 \\
\left|T_-^H T_+^N\right\rangle & 0 & 0 & \frac{-\Delta J_{far}-\Delta J_{near}}{4} & \frac{\Sigma J_{near}-\Sigma J_{far}}{4} & 0 & 0 & 0 & 0 \\
\left|T_+^H T_+^N\right\rangle & 0 & 0 & 0 & 0 & 0 & 0 & 0 & 0 \\
\left|T_-^H T_-^N\right\rangle & 0 & 0 & 0 & 0 & 0 & 0 & 0 & 0 \\
\left|T_0^H T_+^N\right\rangle & 0 & 0 & 0 & 0 & \frac{-\Delta J_{far}-\Delta J_{near}}{4} & \frac{\Sigma J_{near}-\Sigma J_{far}}{4} & 0 & 0 \\
\left|T_+^H T_0^N\right\rangle & 0 & 0 & 0 & 0 & \frac{\Delta J_{far}+\Delta J_{near}}{4} & \frac{\Sigma J_{far}-\Sigma J_{near}}{4} & 0 & 0 \\
\left|T_0^H T_-^N\right\rangle & -\nu_N & \frac{\Sigma J_{near}+\Sigma J_{far}}{4} & 0 & 0 & 0 & 0 & \frac{\Delta J_{far}+\Delta J_{near}}{4} & \frac{\Sigma J_{far}-\Sigma J_{near}}{4} \\
\left|T_-^H T_0^N\right\rangle & \frac{\Sigma J_{near}+\Sigma J_{far}}{4} & -\nu_H & 0 & 0 & 0 & 0 & \frac{-\Delta J_{far}-\Delta J_{near}}{4} & \frac{\Sigma J_{near}-\Sigma J_{far}}{4} \\
\left|S_0^H T_0^N\right\rangle & 0 & 0 & -J_{HH} & \frac{\Delta J_{near}-\Delta J_{far}}{4} & 0 & 0 & 0 & 0 \\
\left|T_0^H S_0^N\right\rangle & 0 & 0 & \frac{\Delta J_{near}-\Delta J_{far}}{4} & -J_{NN} & 0 & 0 & 0 & 0 \\
\left|S_0^H T_+^N\right\rangle & 0 & 0 & 0 & 0 & -J_{HH}+\nu_N & \frac{\Delta J_{near}-\Delta J_{far}}{4} & 0 & 0 \\
\left|T_+^H S_0^N\right\rangle & 0 & 0 & 0 & 0 & \frac{\Delta J_{near}-\Delta J_{far}}{4} & -J_{NN}+\nu_H & 0 & 0 \\
\left|S_0^H T_-^N\right\rangle & \frac{\Delta J_{far}+\Delta J_{near}}{4} & \frac{-\Delta J_{far}-\Delta J_{near}}{4} & 0 & 0 & 0 & 0 & -\nu_N-J_{HH} & \frac{\Delta J_{near}-\Delta J_{far}}{4} \\
\left|T_-^H S_0^N\right\rangle & \frac{\Sigma J_{far}-\Sigma J_{near}}{4} & \frac{\Sigma J_{near}-\Sigma J_{far}}{4} & 0 & 0 & 0 & 0 & \frac{\Delta J_{near}-\Delta J_{far}}{4} & -\nu_H-J_{NN}
\end{array}
$$